



Hydrodynamical Modeling of the Light Curves of Core-collapse Supernovae with HYPERION. I. The Mass Range $13\text{--}25 M_{\odot}$, the Metallicities $-3 \leq [\text{Fe}/\text{H}] \leq 0$, and the Case of SN 1999em

Marco Limongi^{1,2,3} and Alessandro Chieffi^{3,4,5}

¹ INAF—Osservatorio Astronomico di Roma Via Frascati 33, I-00040, Monteporzio Catone, Italy; marco.limongi@inaf.it

² Kavli Institute for the Physics and Mathematics of the Universe, Todai Institutes for Advanced Study, University of Tokyo, Kashiwa, 277-8583 (Kavli IPMU, WPI), Japan

³ INFN. Sezione di Perugia, via A. Pascoli s/n, I-06125 Perugia, Italy

⁴ INAF—Istituto di Astrofisica e Planetologia Spaziali, Via Fosso del Cavaliere 100, I-00133, Roma, Italy

⁵ Monash Centre for Astrophysics (MoCA), School of Mathematical Sciences, Monash University, VIC 3800, Australia

Received 2020 July 16; revised 2020 August 20; accepted 2020 August 31; published 2020 October 15

Abstract

We present the last version of HYdrodynamic Ppm Explosion with Radiation diffUSION (HYPERION), a hydrodynamic code designed to calculate the explosive nucleosynthesis, remnant mass, and light curve associated with the explosion of a massive star. By means of this code, we compute the explosion of a subset of red supergiant models taken from the database published by Limongi & Chieffi for various explosion energies in the range $\sim 0.20\text{--}2.00 \times 10^{51}$ erg. The main outcomes of these simulations, i.e., remnant mass, synthesized ^{56}Ni , luminosity, and length of the plateau of the bolometric light curve, are analyzed as a function of the initial parameters of the star (mass and metallicity) and the explosion energy. As a first application of HYPERION, we estimated the mass and metallicity of the progenitor star of SN 1999em, a well-studied Type IIP supernova, by means of the light-curve fitting. In particular, if the adopted distance to the host galaxy NGC 1637 is 7.83 Mpc, the properties of the light curve point toward a progenitor with an initial mass of $13 M_{\odot}$ and a metallicity $[\text{Fe}/\text{H}] = -1$. If, on the contrary, the adopted distance modulus is 11.7 Mpc, all models with initial mass $13 \leq M/M_{\odot} \leq 15$ and metallicities $-1 \leq [\text{Fe}/\text{H}] \leq 0$ are compatible with the progenitor of SN 1999em.

Unified Astronomy Thesaurus concepts: [Stellar remnants \(1627\)](#); [Core-collapse supernovae \(304\)](#); [Supernova dynamics \(1664\)](#); [Hydrodynamical simulations \(767\)](#); [Hydrodynamics \(1963\)](#)

1. Introduction

Type II supernovae (SNe II) are the end point of the evolution of massive stars that retain an H-rich envelope. Depending on the morphology of their associated light curve, they are generally classified into two broad classes: SNe II-Plateau (or SNe IIP), which show a “plateau” phase lasting typically ~ 100 days where the optical luminosity remains almost constant, and SNe II-Linear (or SNe IIL), which, on the contrary, show a linear decline of the luminosity after the maximum light. Since the mass of the H-rich envelope is the main property of the progenitor star that determines the length of the plateau phase (Grassberg et al. 1971; Falk & Arnett 1977), it has been recently proposed that the transition from SNe IIP to SNe IIL is a continuous process that depends on the mass size of the H-rich envelope, rather than the result of the evolution of two distinct categories of SNe II (Anderson et al. 2014).

The light curves of the SNe IIP are systematically studied for a number of reasons, among which (a) they have been proposed as distance indicators (Kwan & Thuan 1974; Eastman et al. 1996; Jones et al. 2009) with a possible use for cosmology, similar to the SNe Ia, once their basic properties and empirical correlations are known (Chieffi et al. 2003; Nugent et al. 2006; Maguire et al. 2010; Poznanski et al. 2010); and (b) the comparison between the theoretical light curves and the observed ones allows one to derive information on the properties of the progenitor stars (Utrobin 2007; Bersten et al. 2011; Tomasella et al. 2013; Tomasella et al. 2018; Martinez & Bersten 2019), in particular the initial mass and radius. Within the last context, the existence of a tension

between the masses and radii derived from the light-curve fitting and those obtained from the analysis of the archival images acquired prior to the supernova explosion (Davies & Beasor 2018; Martinez & Bersten 2019) has been found in the literature. In general, the masses estimated from the fitting of the light curve are larger than those determined from the analysis of the archival images (Utrobin & Chugai 2008, 2009; Maguire et al. 2010; Morozova et al. 2018). However, in a recent paper, Martinez & Bersten (2019) found that, for a number of SNe IIP, the masses determined from their hydrodynamical modeling are not systematically larger than those previously found in the literature. As a result, the existence of this tension is still debated. Studies on this subject are ongoing, and new developments in both the detection of presupernova progenitors and light-curve modeling are continuously achieved.

On the theoretical side, there are a number of codes, more or less sophisticated, that are currently used to compute the theoretical light curves of SNe IIP. Most of them use a polytrope as a starting model or adopt some kind of parametric procedure (Baklanov et al. 2005; Utrobin 2007; Bersten et al. 2011; Pumo & Zampieri 2011; Martinez & Bersten 2019). In this way, the various properties of the progenitor star (e.g., the total mass, envelope mass, radius, and so on) are assumed as free parameters that may be varied in an independent way. Other codes, on the contrary, follow a more autoconsistent approach, since they adopt as a starting model the one that has passed through the whole presupernova evolution. This obviously means that the various properties of the progenitor star are not free parameters but the result of the presupernova

evolution that, in turn, depends on the initial mass, metallicity, and rotation velocity (Chieffi et al. 2003; Morozova et al. 2015; Sukhbold et al. 2016; Utrobin et al. 2017; Paxton et al. 2018; Dessart & Hillier 2019; Morozova et al. 2020). Note that in the majority of the abovementioned studies, the explosive nucleosynthesis is not taken into account, and the amount of ^{56}Ni that powers the light curve from the plateau phase until the radioactive tail is assumed as a free parameter and deposited by hand in the progenitor model.

This paper is part of a series of works devoted to the study of the presupernova evolution, explosion, and nucleosynthesis of massive stars (Chieffi et al. 1998; Chieffi & Limongi 2004, 2013, 2017; Limongi et al. 2000; Limongi & Chieffi 2003, 2006, 2012, 2018). In these works, great effort has been devoted to the predictions of the chemical composition of the ejecta after the supernova explosion. Since the explosive nucleosynthesis plays a crucial role in the determination of the abundance of most of the isotopes in the ejecta, we developed over the years a hydro code capable of simulating the ejection of the mantle of a massive star due to the explosion and simultaneously computing the explosive nucleosynthesis. Because of the rapid rise and fall of the temperature during the explosion and the high dependence of the cross sections on the temperature, the explosive nucleosynthesis occurs within the first few (1–2) seconds after the core bounce. For this reason, the adoption of the adiabatic approximation is well suited to follow the explosive nucleosynthesis.

In this paper, we present the latest version of this hydro code, which is now named HYPERION (HYdrodynamic Ppm Explosion with Radiation diffusION). The most important upgrade of this code is the inclusion of the treatment of the radiation transport in the flux-limited diffusion approximation. This makes this new version of the code well suited for the calculation of the bolometric light curves of core-collapse supernovae, as well as the explosive nucleosynthesis and remnant mass determination. We use HYPERION to compute the explosions of a subset of models taken from Limongi & Chieffi (2018) that explode as red supergiants with an H-rich envelope. In particular, we consider the mass range 13–25 M_{\odot} and the initial metallicities $[\text{Fe}/\text{H}] = 0, -1, -2, \text{ and } -3$. In this way, we derive the main properties of the light curve (luminosity and length of the plateau, radioactive tail, transition phase, and so on) and the nature of the remnant mass as a function of the properties of the progenitor star (initial mass and metallicity) and the explosion energy. Finally, as a possible application of HYPERION, we fit the observed bolometric light curve of SN 1999em, a well-studied SN IIP, in order to derive the basic properties of its progenitor star.

2. The Code

In this section, we describe in detail the construction and the implementation of HYPERION.

The full system of hydrodynamic equations (written in conservative form), supplemented by the radiative diffusion and the equations describing the temporal variation of the chemical composition due to the nuclear reactions, are written as

$$\frac{\partial \rho}{\partial t} = -4\pi\rho^2 \frac{\partial r^2 v}{\partial m}, \quad (1)$$

$$\frac{\partial v}{\partial t} = -A \frac{\partial P}{\partial m} - \frac{Gm}{r^2}, \quad (2)$$

$$\begin{aligned} \frac{\partial E}{\partial t} &= -\frac{\partial}{\partial m} (AvP + L) + \epsilon, \quad (3) \\ \frac{\partial Y_i}{\partial t} &= \sum_j c_i(j) \Lambda_j Y_j \\ &+ \sum_{j,k} c_i(j,k) \rho N_A \langle \sigma v \rangle_{j,k} Y_j Y_k \\ &+ \sum_{j,k,l} c_i(j,k,l) \rho^2 N_A^2 \langle \sigma v \rangle_{j,k,l} Y_j Y_k Y_l \\ i &= 1, \dots, N, \quad (4) \end{aligned}$$

where ρ is the density, r is the radius, v is the velocity, m is the mass, P is the pressure, $A = 4\pi r^2$, E is the total energy per unit mass (including kinetic, internal, and gravitational), L is the radiative luminosity, and ϵ is any source and/or sink of energy (e.g., nuclear energy production, neutrino losses, and so on). In the last set of N equations, N is the number of nuclear species followed in detail in the calculations, and Y_i is the abundance by number of the i th nuclear species. The different terms in these equations refer to (1) β -decays, electron captures, and photodisintegrations; (2) two-body reactions; and (3) three-body reactions. The coefficients c_i are given by $c_i(j) = \pm N_i$, $c_i(j,k) = \pm N_i / (N_j! N_k!)$, and $c_i(j,k,l) = \pm N_i / (N_j! N_k! N_l!)$, where N_i refers to the number of particles i involved in the reaction, and $N_i!$ prevents double counting for reactions involving identical particles. The sign depends on whether the particle i is produced (+) or destroyed (–); Λ refers to the weak interaction or the photodisintegration rate, while $\langle \sigma v \rangle$ refers to the two- or three-body nuclear cross section. The nuclear network adopted in these calculations includes 335 isotopes (from neutrons to ^{209}Bi ; see Table 1) linked by more than 3000 nuclear reactions.

The nuclear cross sections and weak interaction rates are the ones adopted in Limongi & Chieffi (2018; see their Tables 3 and 4).

In the diffusion approximation, the radiative luminosity is given by

$$L = -(4\pi r^2)^2 \frac{\lambda ac}{3\kappa} \frac{\partial T^4}{\partial m}, \quad (5)$$

where a is the radiation constant, c is the speed of light, κ is the Rosseland mean opacity, and λ is the flux limiter. For this last quantity, we use the expression provided by Levermore & Pomraning (1981),

$$\lambda = \frac{6 + 3R}{6 + 3R + R^2}, \quad (6)$$

where

$$R = \frac{4\pi r^2}{kT^4} \left| \frac{\partial T^4}{\partial m} \right|. \quad (7)$$

The Rosseland mean opacities are calculated assuming a scaled solar distribution of all elements, which for the solar metallicity corresponds to $Z = 1.345 \times 10^{-2}$ according to Asplund et al. (2009). At metallicities lower than solar ($[\text{Fe}/\text{H}] = 0$), we consider an enhancement with respect to Fe of the elements C, O, Mg, Si, S, Ar, Ca, and Ti that is derived from the observations (Cayrel et al. 2004; Spite et al. 2005). As a result of these enhancements, the total metallicity

Table 1
Nuclear Network Adopted in the Present Calculations

Element	A_{\min}	A_{\max}	Element	A_{\min}	A_{\max}
n	1	1	Co	54	61
H	1	3	Ni	56	65
He	3	4	Cu	57	66
Li	6	7	Zn	60	71
Be	7	10	Ga	62	72
B	10	11	Ge	64	77
C	12	14	As	71	77
N	13	16	Se	74	83
O	15	19	Br	75	83
F	17	20	Kr	78	87
Ne	20	23	Rb	79	88
Na	21	24	Sr	84	91
Mg	23	27	Y	85	91
Al	25	28	Zr	90	97
Si	27	32	Nb	91	97
P	29	34	Mo	92	98
S	31	37	Xe	132	135
Cl	33	38	Cs	133	138
Ar	36	41	Ba	134	139
K	37	42	La	138	140
Ca	40	49	Ce	140	141
Sc	41	49	Pr	141	142
Ti	44	51	Nd	142	144
V	45	52	Hg	202	205
Cr	48	55	Tl	203	206
Mn	50	57	Pb	204	209
Fe	52	61	Bi	208	209

corresponding to $[\text{Fe}/\text{H}] = -1, -2, \text{ and } -3$ is $Z = 3.236 \times 10^{-3}, 3.236 \times 10^{-4}, \text{ and } 3.236 \times 10^{-5}$, respectively. For the opacity tables, we use three different sources. In the low-temperature regime ($2.75 < \log T < 4.5$), we use the tables of Ferguson et al. (2005), while in the intermediate-temperature regime ($4.5 < \log T < 8.7$), we adopt the OPAL tables (Iglesias & Rogers 1996). In the high-temperature regime ($8.7 < \log T < 10.0$), we use the Los Alamos Opacity Library (Huebner et al. 1977). Although they are negligible for these calculations, let us mention, for the sake of completeness, that the opacity coefficients due to the thermal conductivity are derived from Itoh et al. (1983). The opacity floor has been computed according to Morozova et al. (2015).

The equation of state (EOS) adopted is the same as described in Morozova et al. (2015). It is based on the analytic EOS provided by Paczynski (1983), which takes into account radiation, ions, and electrons in an arbitrary (approximated) degree of degeneracy. We account for the H and He recombination by solving the Saha equations as proposed by Zaghoul et al. (2000) and assume all other elements are fully ionized.

The nuclear energy generation due to the nuclear reactions has been neglected, under the assumption that this is negligible compared to the other energy components. The energy deposition due to the γ -rays emitted by the radioactive decays $^{56}\text{Ni} \rightarrow ^{56}\text{Co} \rightarrow ^{56}\text{Fe}$, on the contrary, is taken into account following the scheme proposed by Swartz et al. (1995) and Morozova et al. (2015).

The hydrodynamic Equations (1)–(3) are solved by means of the fully Lagrangian scheme of the piecewise parabolic method (PPM) described by Colella & Woodward (1984). This is done in the following three steps. (1) First, we interpolate the profiles

of the variables ρ, v , and P as a function of the mass coordinate by means of the interpolation algorithm described in Colella & Woodward (1984). (2) Then, we solve appropriate Riemann problems at the cell interfaces in order to calculate the time-averaged values of the pressure and velocity at the zone edges. (3) Finally, we update the conserved quantities by applying the forces due to the time-averaged pressures and velocities at the zone edges. In the following, we will describe step (3) in detail.

Let us assume that $\bar{v}_{j+1/2}$ and $\bar{P}_{j+1/2}$ are the solutions of the Riemann problem at the interface between zones j and $j+1$. We first update the radius of the interface $j+1/2$ in the time step $\Delta t = t^{n+1} - t^n$ as

$$r_{j+1/2}^{n+1} = r_{j+1/2}^n + \bar{v}_{j+1/2} \Delta t. \quad (8)$$

Once we know this quantity, we update the time-averaged surface at the zone interface $j+1/2$ according to

$$\bar{A}_{j+1/2} = \frac{4}{3} \pi \frac{(r_{j+1/2}^{n+1})^3 - (r_{j+1/2}^n)^3}{r_{j+1/2}^{n+1} - r_{j+1/2}^n}. \quad (9)$$

The density and velocity of zone j are then updated according to

$$\rho_j^{n+1} = \frac{3 \Delta m_j}{4\pi [(r_{j+1/2}^{n+1})^3 - (r_{j+1/2}^n)^3]}, \quad (10)$$

$$\begin{aligned} v_j^{n+1} &= v_j^n \\ &+ \frac{1}{2} (\bar{A}_{j+1/2} + \bar{A}_{j-1/2}) \frac{\Delta t}{\Delta m_j} (\bar{P}_{j+1/2} - \bar{P}_{j-1/2}) \\ &+ \frac{\Delta t}{2} (g_j^{n+1} + g_j^n), \end{aligned} \quad (11)$$

where $\Delta m_j = m_{j+1/2} - m_{j-1/2}$ is the mass size of zone j , $g_j = Gm_j/r_j^2$ is the gravity, and m_j and r_j are the mass and radius of zone j ; this last quantity is given in general by

$$r_j = \left[\frac{1}{3} \frac{(r_{j+1/2})^3 - (r_{j-1/2})^3}{r_{j+1/2} - r_{j-1/2}} \right]^{1/2}. \quad (12)$$

The equation of the conservation of the total energy is linearized as

$$\begin{aligned} E_j^{n+1} &= E_j^n \\ &- \frac{\Delta t}{\Delta m_j} (\bar{A}_{j+1/2} \bar{v}_{j+1/2} \bar{P}_{j+1/2} - \bar{A}_{j-1/2} \bar{v}_{j-1/2} \bar{P}_{j-1/2}) \\ &- \frac{\Delta t}{\Delta m_j} (L_{j+1/2}^{n+1} - L_{j-1/2}^{n+1}) + \epsilon_j^{n+1} \Delta t. \end{aligned} \quad (13)$$

This equation cannot be solved directly because L^{n+1} and ϵ^{n+1} depend on the updated values of the temperature T^{n+1} (e.g., Equation (5)), which is still unknown at this stage. However, since $E = E_{\text{kin}} + E_{\text{int}} + E_{\text{grav}}$, Equation (13) can be

rewritten as

$$\begin{aligned}
E_{\text{int},j}^{n+1} &= E_{\text{int},j}^n + (E_{\text{kin},j}^n + E_{\text{grav},j}^n - E_{\text{kin},j}^{n+1} + E_{\text{grav},j}^{n+1}) \\
&+ \epsilon_j^{n+1} \Delta t \\
&- \frac{\Delta t}{\Delta m_j} (\bar{A}_{j+1/2} \bar{v}_{j+1/2} \bar{P}_{j+1/2} - \bar{A}_{j-1/2} \bar{v}_{j-1/2} \bar{P}_{j-1/2}) \\
&- \frac{\Delta t}{\Delta m_j} (L_{j+1/2}^{n+1} - L_{j-1/2}^{n+1}).
\end{aligned} \tag{14}$$

The first two terms of Equation (14) are known and do not depend on the updated temperature. In fact, $E_{\text{kin},j}^n$, $E_{\text{int},j}^n$, and $E_{\text{grav},j}^n$ are the values corresponding to the previous model, while $E_{\text{kin},j}^{n+1} = 1/2(v_j^{n+1})^2$ and $E_{\text{grav},j}^{n+1} = -Gm_j/r_j^{n+1}$ depend on variables that are already updated. Also, the third term depends on variables that are already updated, and therefore it is known. In general, $\epsilon = \epsilon_{\text{nuc}} + \epsilon_\nu$, where ϵ_{nuc} is the energy generated by the nuclear reactions, while ϵ_ν is the energy loss due to neutrinos produced by both thermal processes and weak interactions. In this version of the code, we neglect the neutrino losses and the energy produced by nuclear reactions with the exception of the energy produced by the radioactive decay of $^{56}\text{Ni} \rightarrow ^{56}\text{Co} \rightarrow ^{56}\text{Fe}$, i.e., $\epsilon_{\text{nuc}} = \epsilon_{^{56}\text{Ni}}$. This last quantity is computed as mentioned above and does not depend on the updated value of the temperature.

Thus, defining the quantities

$$\begin{aligned}
C_j &= E_{\text{int},j}^n + (E_{\text{kin},j}^n + E_{\text{grav},j}^n - E_{\text{kin},j}^{n+1} + E_{\text{grav},j}^{n+1}) \\
&- \frac{\Delta t}{\Delta m_j} (\bar{A}_{j+1/2} \bar{v}_{j+1/2} \bar{P}_{j+1/2} - \bar{A}_{j-1/2} \bar{v}_{j-1/2} \bar{P}_{j-1/2})
\end{aligned} \tag{15}$$

and

$$G_j = E_{\text{int},j}^n + C_j + \epsilon_{^{56}\text{Ni},j}^{n+1} \Delta t, \tag{16}$$

Equation (14) can be rewritten as

$$E_{\text{int},j}^{n+1} = G_j - \frac{\Delta t}{\Delta m_j} (L_{j+1/2}^{n+1} - L_{j-1/2}^{n+1}), \tag{17}$$

with G_j constant and defined at the zone center.

According to Equation (5), the luminosity, defined at the zone interfaces, can be linearized as

$$\begin{aligned}
L_{j+1/2}^{n+1} &= -\bar{A}_{j+1/2}^2 \left(\frac{1}{\kappa_{j+1/2}} \right)^{n+1} \frac{ac \chi_{j+1/2}^{n+1}}{3} \\
&\times \frac{(T_{j+1}^{n+1})^4 - (T_j^{n+1})^4}{m_{j+1} - m_j}.
\end{aligned} \tag{18}$$

The opacity κ depends on the temperature and density; therefore, it is naturally defined at the zone center. For this reason, we define the value $\kappa_{j+1/2}$ of the opacity at the zone interface as described in Morozova et al. (2015):

$$\left(\frac{1}{\kappa_{j+1/2}} \right)^{n+1} = \frac{(T_{j+1}^{n+1})^4 / \kappa_{j+1}^{n+1} + (T_j^{n+1})^4 / \kappa_j^{n+1}}{(T_{j+1}^{n+1})^4 + (T_j^{n+1})^4}. \tag{19}$$

According to Equations (6) and (7), the flux limiter λ is given by

$$\lambda_{j+1/2}^{n+1} = \frac{6 + 3R_{j+1/2}^{n+1}}{6 + 3R_{j+1/2}^{n+1} + (R_{j+1/2}^{n+1})^2}, \tag{20}$$

where

$$\begin{aligned}
R_{j+1/2}^{n+1} &= \frac{2\bar{A}_{j+1/2}}{m_{j+1} - m_j} \\
&\times \frac{|(T_{j+1}^{n+1})^4 - (T_j^{n+1})^4| \left(\frac{1}{\kappa_{j+1/2}} \right)^{n+1}}{(T_{j+1}^{n+1})^4 + (T_j^{n+1})^4}.
\end{aligned} \tag{21}$$

By means of Equations (18)–(21), and since $E_{\text{int},j}^{n+1}$ depends on ρ_j^{n+1} and T_j^{n+1} , it is easy to verify that Equation (17) depends only on T_{j-1}^{n+1} , T_j^{n+1} , and T_{j+1}^{n+1} . If the number of zones is M , assuming for the boundary conditions that $L_{-1/2} = 0$ and $L_{M+1/2} = L_{M-1/2}$, Equation (17) written for all the zones produces a system of M equations for the M unknowns T_j^{n+1} ($j = 1, \dots, M$) that is solved by means of a Newton–Raphson method. In particular, assuming a trial value for the temperature T_j^{n+1} ($j = 1, \dots, M$), this algorithm implies the solution of the following system:

$$\begin{aligned}
\frac{\partial E_{\text{int},j}^{n+1}}{\partial T_j} \Delta T_j - \frac{\Delta t}{\Delta m_j} \left(\frac{\partial L_{j+1/2}^{n+1}}{\partial T_{j+1}} \Delta T_{j+1} + \frac{\partial L_{j+1/2}^{n+1}}{\partial T_j} \Delta T_j \right) \\
- \left(\frac{\partial L_{j-1/2}^{n+1}}{\partial T_j} \Delta T_j - \frac{\partial L_{j-1/2}^{n+1}}{\partial T_{j-1}} \Delta T_{j-1} \right) = -\delta_j,
\end{aligned} \tag{22}$$

where

$$\delta_j = E_{\text{int},j}^{n+1} - G_j + \frac{\Delta t}{\Delta m_j} (L_{j+1/2}^{n+1} - L_{j-1/2}^{n+1}). \tag{23}$$

The derivative of the internal energy with respect to the temperature is obtained from the EOS, while the derivatives of the luminosity can be computed according to Equation (18):

$$\begin{aligned}
\frac{\partial L_{j+1/2}^{n+1}}{\partial T_{j+1}} &= -\bar{A}_{j+1/2}^2 \left(\frac{1}{\kappa_{j+1/2}} \right)^{n+1} \\
&\times \frac{4ac \chi_{j+1/2}^{n+1} (T_{j+1}^{n+1})^3}{3 (m_{j+1} - m_j)},
\end{aligned} \tag{24}$$

$$\begin{aligned}
\frac{\partial L_{j+1/2}^{n+1}}{\partial T_j} &= +\bar{A}_{j+1/2}^2 \left(\frac{1}{\kappa_{j+1/2}} \right)^{n+1} \\
&\times \frac{4ac \chi_{j+1/2}^{n+1} (T_j^{n+1})^3}{3 (m_{j+1} - m_j)},
\end{aligned} \tag{25}$$

$$\begin{aligned}
\frac{\partial L_{j-1/2}^{n+1}}{\partial T_j} &= -\bar{A}_{j-1/2}^2 \left(\frac{1}{\kappa_{j-1/2}} \right)^{n+1} \\
&\times \frac{4ac \chi_{j-1/2}^{n+1} (T_j^{n+1})^3}{3 (m_j - m_{j-1})},
\end{aligned} \tag{26}$$

$$\frac{\partial L_{j-1/2}^{n+1}}{\partial T_j} = \bar{A}_{j-1/2}^2 \left(\frac{1}{\kappa_{j-1/2}} \right)^{n+1} \times \frac{4ac\chi_{j-1/2}^{n+1} (T_{j-1}^{n+1})^3}{3 m_j - m_{j-1}}. \quad (27)$$

In this case, we neglect the derivatives of the opacity as a function of the temperature.

Therefore, the matrix of the coefficient of the system (Equation (23)), rewritten as

$$\begin{aligned} & \frac{\Delta t}{\Delta m_j} \frac{\partial L_{j-1/2}^{n+1}}{\partial T_{j-1}} \Delta T_{j-1} \\ & + \left[\frac{\partial E_{\text{int},j}^{n+1}}{\partial T_j} - \frac{\Delta t}{\Delta m_j} \left(\frac{\partial L_{j+1/2}^{n+1}}{\partial T_j} - \frac{\partial L_{j-1/2}^{n+1}}{\partial T_j} \right) \right] \Delta T_j \\ & - \frac{\Delta t}{\Delta m_j} \frac{\partial L_{j+1/2}^{n+1}}{\partial T_{j+1}} \Delta T_{j+1} = -\delta_j, \end{aligned} \quad (28)$$

is a tridiagonal band matrix like

$$\begin{bmatrix} b_1 & c_1 & 0 & \cdots & 0 \\ a_2 & b_2 & c_2 & & \vdots \\ 0 & \ddots & \ddots & \ddots & 0 \\ \vdots & & a_{M-1} & b_{M-1} & c_{M-1} \\ 0 & \cdots & 0 & a_M & b_M \end{bmatrix}, \quad (29)$$

where

$$a_j = \frac{\Delta t}{\Delta m_j} \frac{\partial L_{j-1/2}^{n+1}}{\partial T_{j-1}}, \quad (30)$$

$$b_j = \frac{\partial E_{\text{int},j}^{n+1}}{\partial T_j} - \frac{\Delta t}{\Delta m_j} \left(\frac{\partial L_{j+1/2}^{n+1}}{\partial T_j} - \frac{\partial L_{j-1/2}^{n+1}}{\partial T_j} \right), \quad (31)$$

$$c_j = -\frac{\Delta t}{\Delta m_j} \frac{\partial L_{j+1/2}^{n+1}}{\partial T_{j+1}}. \quad (32)$$

To invert this matrix, we use the SPARSEKIT2 package (Yousef Saad website; <https://www-users.cs.umn.edu/saad/software/SPARSKIT/>). Once the system is solved, the initial trial values of the temperature are updated, e.g., $T_j^{n+1} \rightarrow T_j^{n+1} + \Delta T_{j+1}$, and the process is repeated until both the equations and the normalized corrections $\frac{\Delta T}{T}$ become less than a chosen tolerance.

By means of the updated values of the temperature and density in each zone, the system of Equation (4) is solved with the Newton–Raphson method in order to compute the updated values of the abundances of all nuclear species included in the nuclear network (Table 1).

The PPM algorithm described above assumes the presence of six ghost zones at the inner and outer boundaries of the computation domain. At the inner edge, we impose reflecting boundary conditions, which means that all of the various quantities in the ghost zones are defined as

$$a_{7-j} = \pm a_{7+j-1} \quad j = 1, \dots, 6, \quad (33)$$

where the sign is negative for velocity and positive for all other quantities. At the outer edge of the computation domain, we assume that all quantities in the ghost zones are kept constant and equal to the values of the last “real” zone, with the

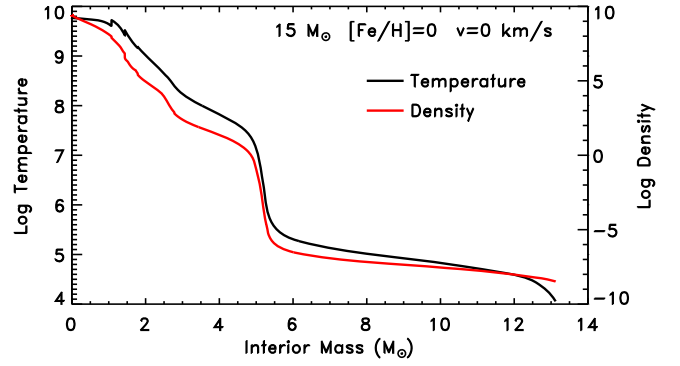


Figure 1. Temperature and density profiles as a function of the interior mass at the presupernova stage of model 15a.

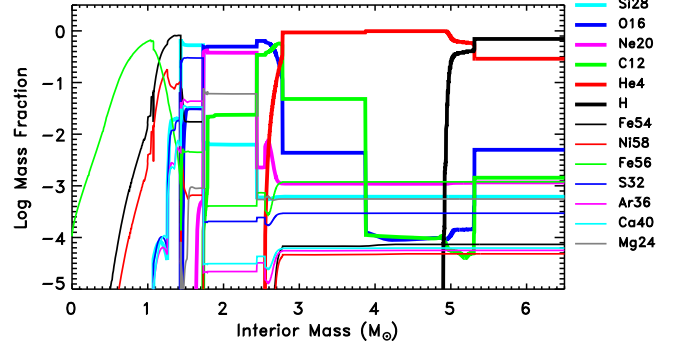


Figure 2. Chemical composition as a function of the interior mass at the presupernova stage of model 15a. The most abundant nuclei in the inner zones of the Fe core, e.g., the neutron-rich isotopes ^{50}Ti , ^{54}Cr , ^{60}Fe , ^{64}Ni , and so on, are not shown.

exception of the pressure, which is set to a fixed value corresponding to 10^{-24} dyne cm^{-2} .

3. Explosion and Light Curve of a Typical Case

In this section, we describe in detail the main properties of the explosion and the light curve of a model that we consider typical, i.e., a solar metallicity nonrotating $15 M_{\odot}$ (model 15a). The explosion, computed by means of HYPERION (Section 2), is induced by removing the inner $0.8 M_{\odot}$ of the presupernova model and instantaneously depositing a given amount of thermal energy in the inner $0.1 M_{\odot}$ (i.e., in the region between 0.8 and $0.9 M_{\odot}$). The energy deposited is chosen in order to have a final explosion energy (mainly in the form of kinetic energy of the ejecta) $E_{\text{expl}} \simeq 1.0$ foe ($1 \text{ foe} = 10^{51}$ erg). Such an artificial way of inducing the explosion is due to the lack of a routine way of computing a self-consistent multidimensional explosion of a massive star, and it constitutes the typical technique, with few small variations, adopted to calculate explosive nucleosynthesis and remnant masses of core-collapse supernovae (Woosley & Weaver 1995; Thielemann et al. 1996; Umeda & Nomoto 2002; Limongi & Chieffi 2003; Heger & Woosley 2010). A detailed explanation of how the nucleosynthesis and remnant masses depend on the explosion parameters can be found in Aufderheide et al. (1991) and Umeda & Yoshida (2017, and references therein). Let us only remark that, at variance with the other similar calculations, we choose an initial mass cut internal enough that the properties of the shock wave, at the time it reaches the iron core edge, mildly depend on the initial conditions. Figures 1 and 2 show,

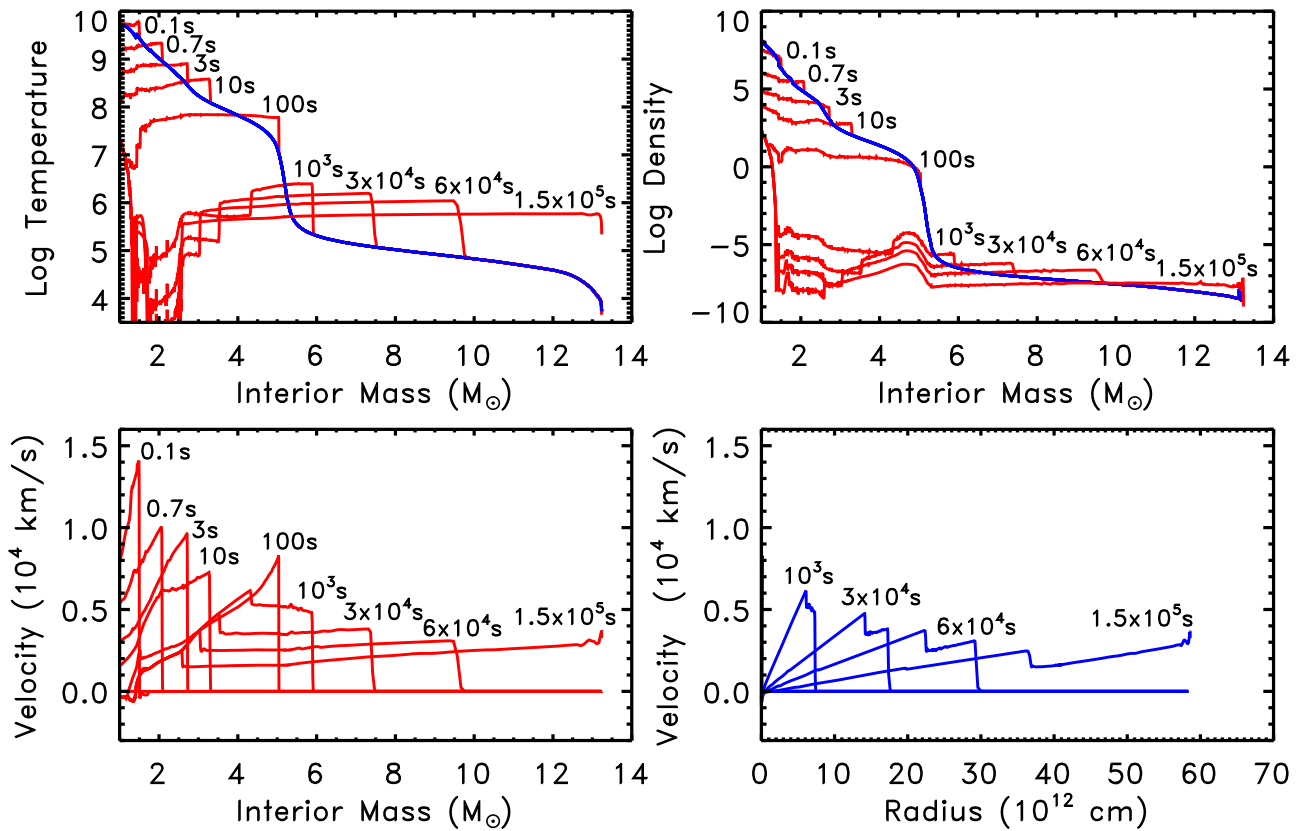


Figure 3. Main physical and chemical properties of model 15a at various times during the explosion.

respectively, the temperature plus density profiles and the chemical composition of the star at the presupernova stage.

3.1. Propagation of the Shock Wave, Explosive Nucleosynthesis, Fallback, and Shock Breakout

The injection of thermal energy into the model heats, compresses, and accelerates the overlying layers, inducing a progressive conversion of the internal energy into kinetic energy so that a shock wave forms and begins to propagate outward. The temperature behind the shock is almost constant, as expected when radiation dominates the energy budget, and reaches values high enough ($\gtrsim 7 \times 10^9$ K) to trigger explosive nucleosynthesis (Figure 3, upper panels).

The inner zone between the edge of the iron core and $\sim 1.55 M_{\odot}$ is exposed to the highest temperature ($T \geq 5$ GK), undergoes explosive Si burning with complete Si exhaustion, and is dominated by ^{56}Ni (^{56}Fe), which is by far the most abundant nuclear species (the total ^{56}Ni ejected in this model is $0.126 M_{\odot}$). Other abundant isotopes in this zone are ^{58}Ni , ^{57}Ni (^{57}Fe), ^{60}Zn (^{60}Ni), ^{62}Zn (^{62}Ni), and ^4He (the unstable nuclei will decay at late times into their parent stable isotopes, reported in parentheses; Figure 4).

The layers between ~ 1.55 and $\sim 1.69 M_{\odot}$ undergo explosive Si burning with incomplete Si exhaustion (peak temperature $5 \text{ GK} \geq T \geq 4 \text{ GK}$) and are mainly loaded with the iron peak elements ^{56}Ni , ^{58}Ni , ^{57}Ni (^{57}Fe), ^{54}Fe , ^{55}Co (^{55}Mn), and ^{52}Fe (^{52}Cr) and the α nuclei ^{32}S , ^{40}Ca , ^{36}Ar , and ^{28}Si (the one that remains partially unburned; Figure 5).

Explosive O burning occurs in the region between ~ 1.70 and $\sim 1.77 M_{\odot}$ (peak temperature $4 \text{ GK} \geq T \geq 3.2 \text{ GK}$) and

produces mainly the α nuclei ^{28}Si , $^{32,34}\text{S}$, $^{36,38}\text{Ar}$, and ^{40}Ca (Figure 6).

Explosive Ne burning occurs in the zones between ~ 1.77 and $\sim 2.10 M_{\odot}$ (peak temperature $3.2 \text{ GK} \geq T \geq 2.0 \text{ GK}$) and produces or partially modifies (destroys or produces) the preexplosive abundances of ^{16}O , ^{20}Ne , ^{23}Na , $^{24,25,26}\text{Mg}$, ^{27}Al , $^{28,29,30}\text{Si}$, and ^{31}P (Figure 7).

Explosive C burning occurs where the peak temperature of the shock wave reaches $\sim 2.0 \times 10^9$ K (Figure 3), and this happens at the mass coordinate of $\sim 2.1 M_{\odot}$ (Figure 2). Note that the products of this explosive burning are almost negligible, in this specific case, because of the very low ^{12}C mass fraction present in the C convective shell. This mass coordinate is reached by the shock wave ~ 0.7 s after the start of the explosion, and this time it marks the end of the explosive burning, since beyond this mass, the peak temperature of the shock wave becomes too low to trigger additional burning. At this time, the velocity of the shocked zones ranges between $\sim 0.6 \times 10^4$ and $\sim 10^4 \text{ km s}^{-1}$ (Figure 3, lower left panel).

Roughly 3 s after the beginning of the explosion, the shock wave reaches the edge of the CO core. At this time, the temperature and density of the shock have decreased to $\sim 6 \times 10^8$ K and $\sim 10^4 \text{ g cm}^{-3}$, respectively, while the velocity of the shocked layers ranges between $\sim 0.3 \times 10^4$ and $\sim 10^4 \text{ km s}^{-1}$ (Figure 3, lower left panel). Figure 8 shows the run of the internal (red), kinetic (green), and total (black) energy within the expanding ejecta at four key points. The upper left panel in the figure refers to $t = 3$ s. Already at this point, the kinetic energy of many layers becomes comparable to, or even larger than, the internal one.

Roughly 10 s after the beginning of the explosion, some of the most internal layers revert their velocity because they are

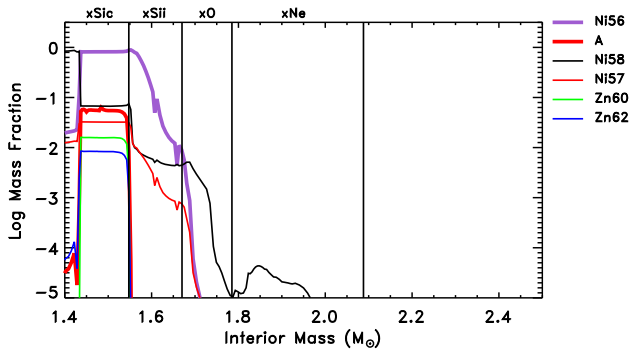


Figure 4. Profile of the most abundant isotopes produced by the explosive Si burning with complete Si exhaustion in the zone between the edge of the iron core and $\sim 1.55 M_{\odot}$.

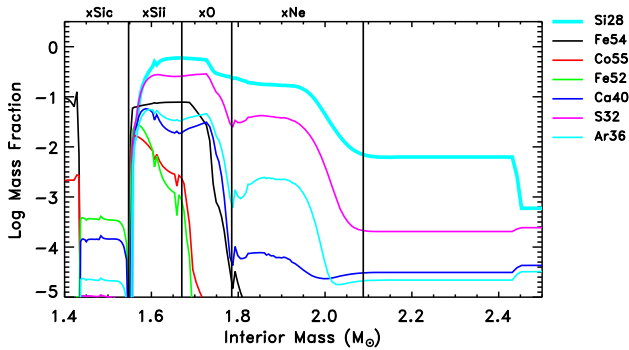


Figure 5. Profile of the most abundant isotopes produced by the explosive Si burning with incomplete Si exhaustion in the zone between ~ 1.55 and $\sim 1.69 M_{\odot}$.

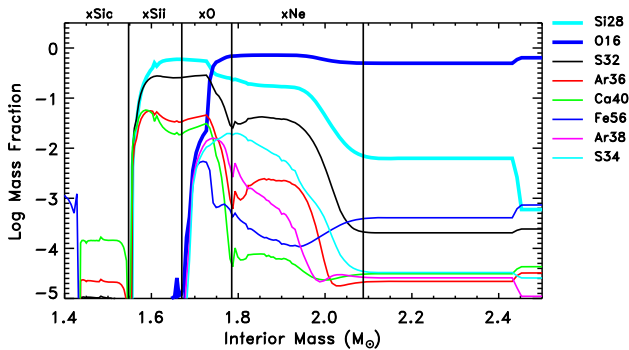


Figure 6. Profile of the most abundant isotopes produced by the explosive O burning in the zone between ~ 1.70 and $\sim 1.77 M_{\odot}$.

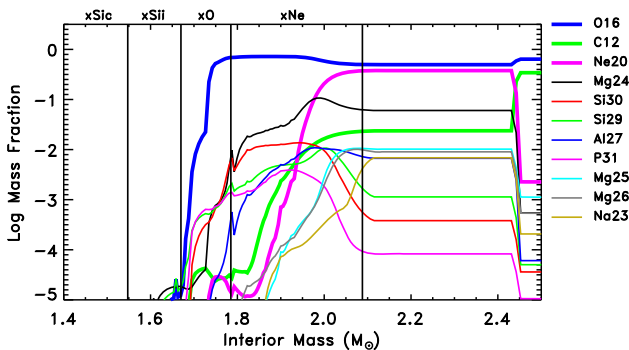


Figure 7. Profile of the most abundant isotopes produced by the explosive Ne burning in the zone between ~ 1.77 and $\sim 2.10 M_{\odot}$.

not able to reach the escape velocity; therefore, they fall back onto the compact remnant. Almost $0.45 M_{\odot}$ of the initial ejecta collapses back in the initial remnant, increasing the mass cut, i.e., the mass coordinate that divides the remnant from the ejecta, to $\sim 1.25 M_{\odot}$.

In ~ 100 s, the shock wave reaches the He/H interface, where a strong density gradient is present (Figure 1). Most of the internal energy behind the shock has been converted into kinetic energy that now dominates the total energy (Figure 8, upper right panel), while the gravitational energy becomes negligible in this region. The presence of the strong density gradient at the He/H interface induces the formation of a reverse shock (see, e.g., Woosley & Weaver 1995), so that from this time onward, the explosion is characterized by a forward shock that continues to propagate outward and a reverse shock that propagates inward in mass and slows down the material previously accelerated by the forward shock (Figure 3).

As the two shocks move away from each other, the temperature remains almost constant in the region between the two, while the density shows a bump close to the H/He interface that will persist up to the late stages and have some important consequences for the features of the light curve during the transition from the plateau phase to the radioactive tail (see below). Both the temperature and the density decrease, maintaining their shape as time goes by. During this phase, additional internal zones fall back onto the compact remnant because of the interaction with the reverse shock. This process eventually ends $\sim 10^4$ s after the onset of the explosion, leaving a final compact remnant of $\sim 1.42 M_{\odot}$. Note that such a fallback brings back part of the matter where explosive Si burning with complete Si exhaustion occurred and most of the ^{56}Ni and many iron peak nuclei are synthesized (Figure 4), preventing their ejection into the interstellar medium.

The forward shock eventually reaches the surface of the star $\sim 1.5 \times 10^5$ s (~ 1.7 days) after the onset of the explosion, and at this stage, the reverse shock has moved down to $\sim 2.5 M_{\odot}$. When the shock wave reaches the surface, both the temperature and the bolometric luminosity increase to $\sim 2 \times 10^5$ K and $\sim 2 \times 10^{45}$ erg s^{-1} , respectively (Figure 9), and the expanding mantle is totally ionized, since the temperature exceeds $\sim 10^5$ K everywhere.

Before closing this subsection, let us remark that once the main shock wave overturns the H/He interface, the total energy in the shocked part of the H-rich mantle is dominated by the kinetic energy, while it is basically equiparted between internal and kinetic within the He core (Figure 8, lower right panel).

3.2. Adiabatic Cooling

The first phase of expansion of the ejecta (i.e., between 1.7 and 18 days) is characterized by a few phenomena worth recalling.

First, the velocity of the various layers after the breakout (Figure 3, lower right panel) does not remain frozen because the internal energy still feeds the kinetic energy. Figure 10 shows the temporal evolution of both the kinetic and internal energies of the ejecta. The kinetic energy increases from 0.6 (the value at the breakout) to 0.9 foe in the first 3.5 days after the breakout (~ 5 days from the explosion), increasing up to almost the final value of 1 foe in the other 13 days (~ 18 days from the explosion).

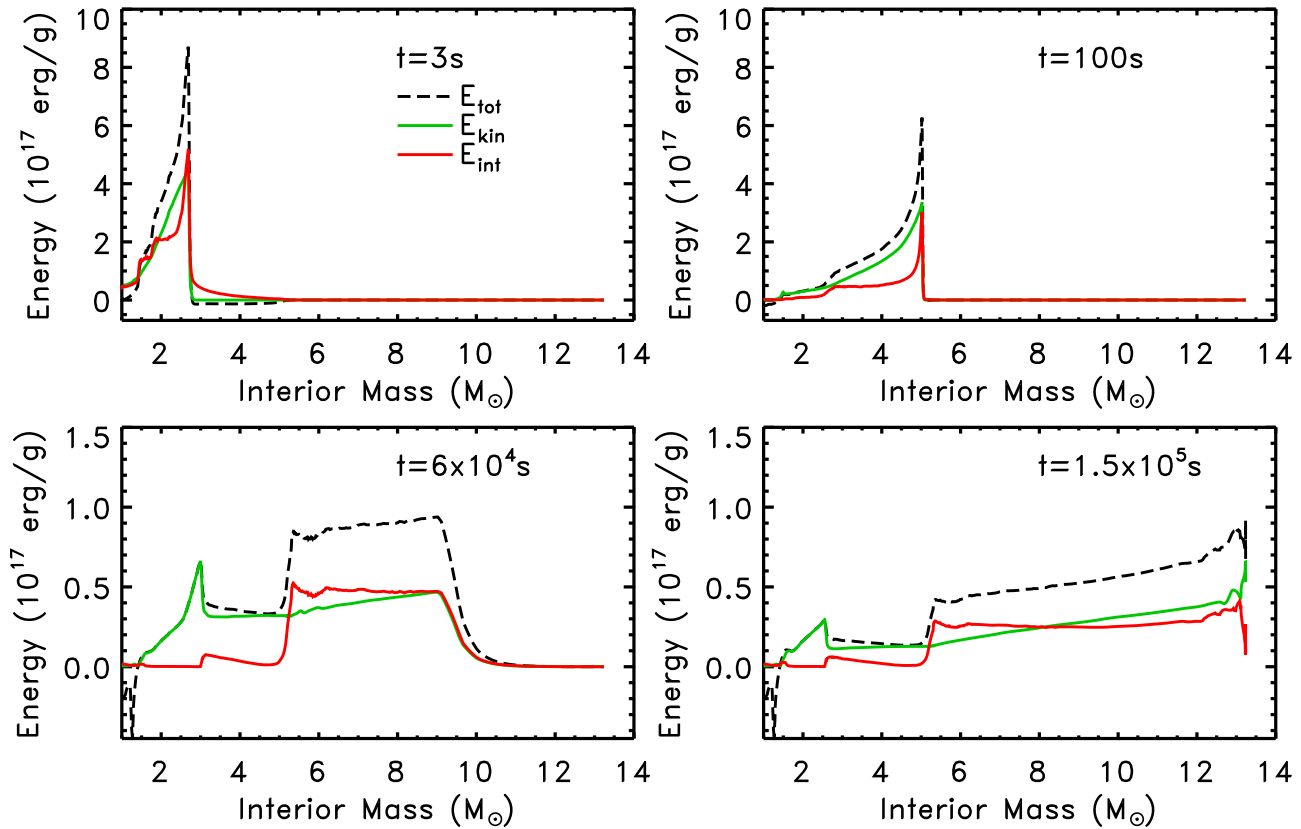


Figure 8. Interior profiles of the total (black line), kinetic (green line), and internal (red line) energy at various times during the explosion.

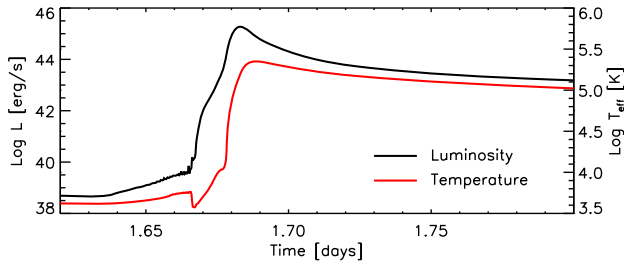


Figure 9. Evolution of the bolometric luminosity and effective temperature of model 15a with $E_{\text{rmet}} = 1.0$ foe during the breakout.

The second thing worth recalling is that the decrease of the internal energy is initially due almost exclusively to adiabatic expansion, while the radiative losses prevail at a later time. This is clearly visible in Figure 11. From the first law of thermodynamics, we have $\dot{E} = -P\dot{V} - \partial L/\partial m$, where E is the internal energy per unit mass and we have neglected any other source term for the moment; the other terms have the usual meaning. The figure clearly shows that more than 90% of the internal energy losses are due to the $P\dot{V}$ term, at least up to day ~ 18 , and therefore that the expansion is essentially adiabatic, i.e., $\dot{E} \simeq -P\dot{V}$, in this phase.

The temperature within the whole expanding mantle is well above 10^5 K, so that matter is fully ionized everywhere, an occurrence that prevents it from becoming transparent to the radiation. As a consequence, the surface of the expanding mantle (defined as the mass coordinate where $\tau = 2/3$) remains basically anchored at the same mass coordinate. Figure 12 shows the velocity of selected layers together with the location of the photosphere. It is clearly visible that in the first 18 days or so, the mass coordinate of the photosphere does

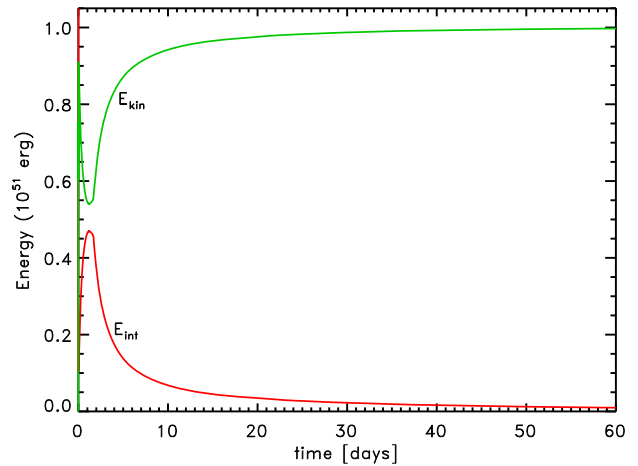


Figure 10. Evolution of the total internal (red line) and kinetic (green line) energies. The maximum of the internal energy (minimum of the kinetic energy) corresponds to the time of the shock breakout. Note that, as is mentioned in the text, at the time of the shock breakout, the total energy ($\sim 10^{51}$ erg = 1 foe) is roughly divided into equal proportions between internal and kinetic energy.

not change significantly. The temporal evolution of the surface luminosity (by definition, the luminosity of the photosphere) follows the behavior of the photosphere itself. Here L is approximately proportional to $R^2 T^4$ (where R and T refer to the radius of the photosphere); since, in an adiabatic expansion of a radiation-dominated gas, $\dot{E} \simeq -P\dot{V}$ implies $T \propto R^{-1}$, T^4 scales as R^{-4} and hence $L \propto 1/R^2$. This explains the initial decline of the luminosity after the breakout. Figure 13 shows the evolution of the bolometric luminosity as a red line. The adiabatic cooling phase goes from the breakout to the beginning of a phase in

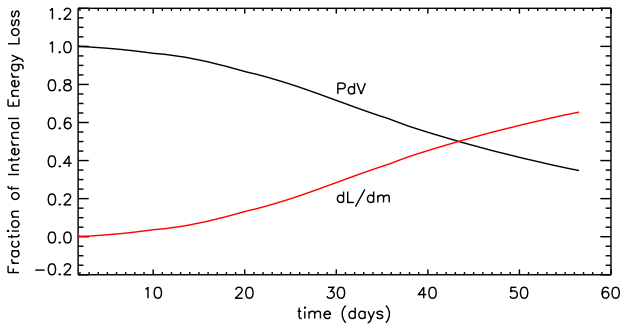


Figure 11. Fraction of internal energy loss due to adiabatic cooling ($P\dot{V}/\dot{E}$; black line) and radiative losses ($\partial L/\partial m/\dot{E}$; red line).

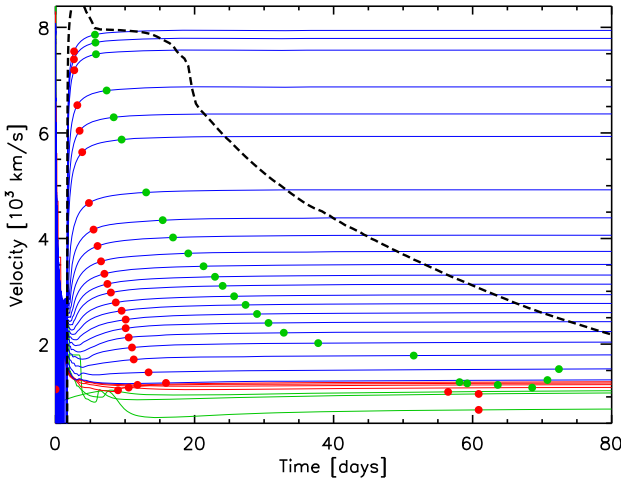


Figure 12. Evolution of the velocity of selected layers with time. The red and green dots mark the times when the layer reaches 95% and 99% of its terminal velocity, respectively. The blue, red, and green lines mark the H-, He-, and CO-rich layers, respectively. The black dashed line is the velocity of the photosphere.

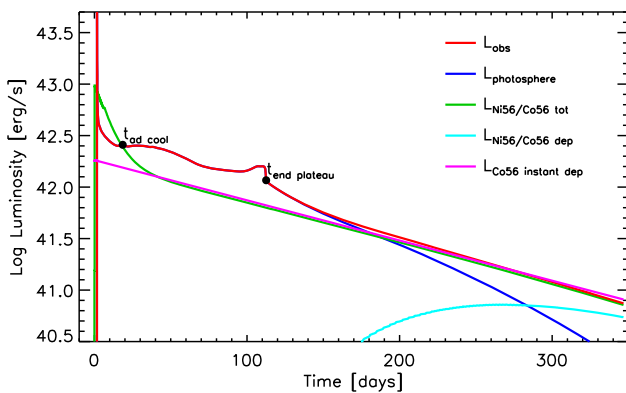


Figure 13. Bolometric observed luminosity (red line), luminosity at the photosphere (blue line), total luminosity due to $^{56}\text{Ni}/^{56}\text{Co}$ decay (green line), luminosity due to the absorption of γ -rays from $^{56}\text{Ni}/^{56}\text{Co}$ decay above the photosphere (cyan line), and instantaneous energy deposition by radioactive ^{56}Co decay (magenta line) corresponding to $0.126 M_{\odot}$ of initially synthesized ^{56}Ni as a function of the time elapsed from the explosion (Nadyozhin 1994, Equation (19)).

which the surface luminosity is roughly constant (marked by a black dot). This change of behavior will be discussed in the next section.

As already mentioned above, at day ~ 18 , all of the ejecta have almost reached their terminal velocity (Figure 12), and hence the following evolution is characterized by a free

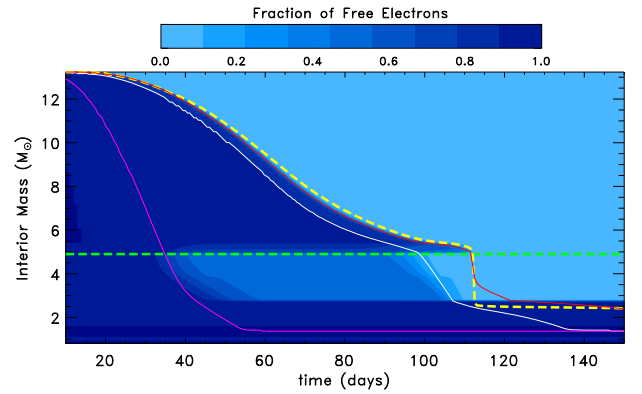


Figure 14. Fraction of free electrons as a function of time (x-axis) and interior mass (y-axis) according to the color coding reported in the color bar on top of the plot. The yellow dashed line marks the location of the photosphere, and the red, white, and magenta lines mark the layers where the recombination temperatures for H II, He II, and He III are achieved, respectively. The horizontal dashed green line marks the H/He interface.

expansion where forces due to the pressure gradient and gravitation are now negligible. In this regime, the expansion becomes homologous, i.e., characterized by a constant velocity of each layer that scales linearly with the radius. Note that the more internal zones are the last to achieve this stage because the reverse shock reaches the base of the expanding envelope only ~ 10 days after the explosion.

3.3. Recombination Front and Plateau Phase

The phase of adiabatic expansion of the ejecta ends at day ~ 18 , i.e., when the temperature of the photosphere drops to ~ 5500 K and the H recombines. Since the opacity is mainly due to the electron scattering, it decreases dramatically in these zones, increasing their transparency to radiation. As a consequence, the internal energy is radiated away very efficiently, and the temperature drops abruptly at the recombination front. Such an occurrence marks the end of the phase in which the photosphere remains anchored to the most external layer of the ejecta. In fact, as the expansion proceeds, the temperature of a progressively increasing number of (more internal) zones drops below the critical value for the H recombination and, as a consequence, a cooling wave, due to the transparency induced by the recombination front, progressively penetrates inward in mass. The strong reduction of the opacity implies a strong reduction of the optical depth; therefore, the location of the photosphere, defined as the first layer where $\tau = 2/3$, closely follows the recombination wave. For the sake of simplicity, in the following, we will consider the recombination front and the photosphere coincident in mass.

Figures 14–16 map the temporal evolution of the fraction of free electrons, the opacity, and the temperature inside the star, respectively. These first two plots clearly show that the opacity drops whenever the fraction of free electrons reduces. Moreover, the three solid lines in Figure 14, marking the location where He III (magenta), He II (white), and H II (red) recombine, show that the recombination of He III obviously occurs first. Such an occurrence, however, does not appreciably affect the fraction of free electrons (and hence the opacity) in the H-rich envelope because in this zone, that fraction is mainly determined by the hydrogen itself. For this reason, in the first ~ 18 days, the fraction of free electrons does not change

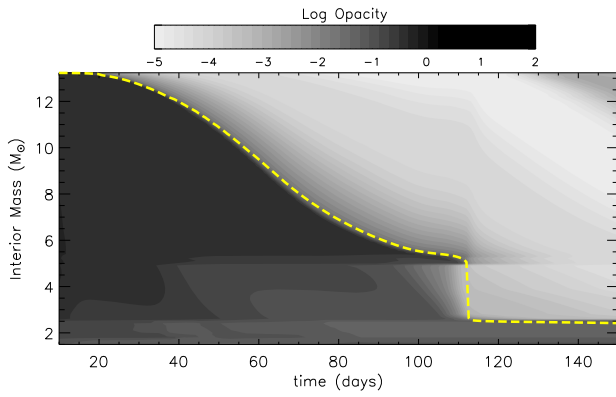


Figure 15. Opacity as a function of time (x-axis) and interior mass (y-axis) according to the color coding reported in the color bar on top of the plot. The yellow dashed line marks the location of the photosphere.

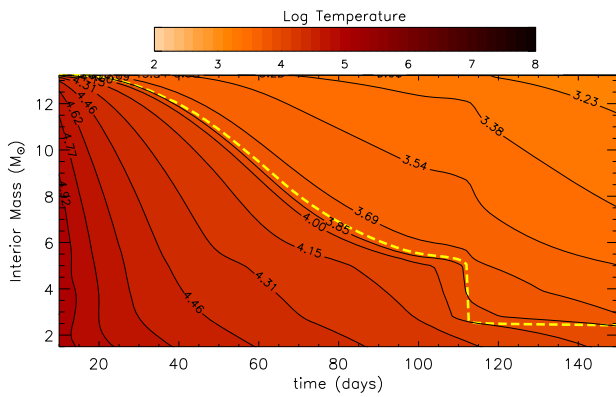


Figure 16. Temperature as a function of time (x-axis) and interior mass (y-axis) according to the color coding reported in the color bar on top of the plot. The contour levels are also plotted. The yellow dashed line marks the location of the photosphere.

appreciably in any layer of the star. Roughly at day 18, H begins to recombine and the photosphere starts moving inward, leaving outside matter with a very low fraction of free electrons and hence a low opacity. It is worth noting that in this phase, the photosphere (yellow dashed line) closely follows the isothermal corresponding to the H recombination temperature (Figure 16).

Around day 40, the temperature in the He core drops below the threshold value for He III recombination first (and for He II later), and this determines a strong reduction of the number of free electrons (and of the opacity) within the He core (see Figures 14 and 15). Once the photosphere reaches the H/He interface (at day ~ 110), it very quickly shifts down to the CO core because of the very low opacity between the CO core and the H/He interface. The fraction of free electrons remains equal to 1 within the CO core because we assume that matter remains fully ionized in the He-exhausted zone (see Section 2).

Figure 17 shows the typical relative contributions of the adiabatic cooling (red line), radiative losses (green line), and ^{56}Ni radioactive decay (blue line) to the variation of the internal energy in the phase in which the recombination front moves within the H-rich mantle (the figure is a snapshot taken at day ~ 35). The figure shows very clearly that behind the recombination front (marked by the magenta vertical dashed line), the cooling due to the adiabatic expansion (red line)

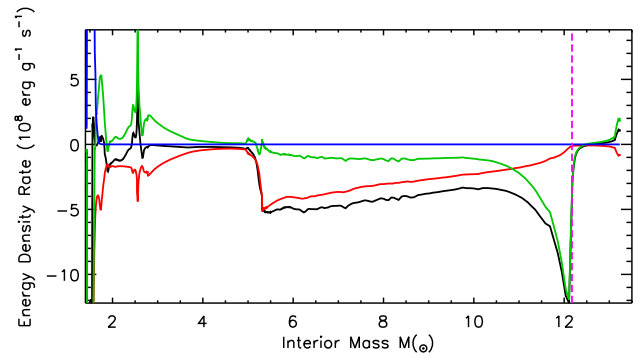


Figure 17. Time derivative of the internal energy per unit mass (\dot{E}) as a function of interior mass (black line) for a model at day ~ 35 . The contribution due to the adiabatic expansion ($P\dot{V}$), radiative diffusion (dL/dm), and ^{56}Ni radioactive decay are shown with red, green, and blue lines, respectively. The magenta vertical dashed line marks the location of the photosphere.

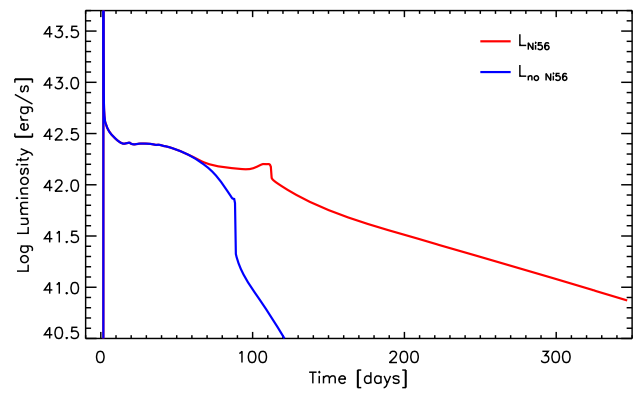


Figure 18. Comparison between the reference light curve (red line) and the one obtained by artificially setting the abundance of ^{56}Ni (blue line) to zero.

dominates the energy losses up to $\sim 10 M_{\odot}$, while the radiative losses dominate close to the photosphere and beyond.

The surface luminosity levels off after the first phase of adiabatic expansion and maintains a roughly flat profile until the recombination front reaches the H/He discontinuity (Figure 13). The reason is that both its radius and temperature do not vary significantly in this phase. Since the expansion of the mantle behind the recombination front is almost adiabatic (see Figure 17), the temperature of each layer scales as $T \simeq R^{-1}$, and since the recombination temperature is roughly fixed (at ~ 5500 K), the recombination radius remains practically frozen at a constant value. It must be noted that the release of energy coming from the cascade decay of ^{56}Ni contributes to determining the duration of the plateau phase. The contribution of $^{56}\text{Ni} \rightarrow ^{56}\text{Co}$ decay to sculpting the shape of the light curve in the plateau phase, in particular its duration, is clearly shown in Figure 18, where the light curve of the reference model (red line) is compared to one computed by artificially switching off the cascade decay of ^{56}Ni (blue line).

The luminosity profile in the transition from the plateau phase to the radioactive tail depends on a complex interplay among the temporal evolution of temperature, density, and chemical composition. We will discuss how this interplay affects both the slope of the luminosity profile and the formation of a luminosity bump in this transition phase in Section 3.5.

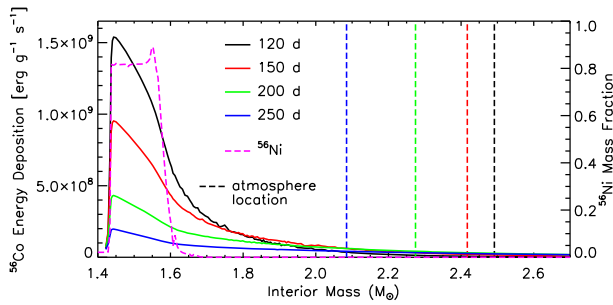


Figure 19. Energy deposition ($\text{erg g}^{-1} \text{s}^{-1}$) due to ^{56}Co radioactive decay as a function of interior mass at various times (solid lines, primary y-axis) after the explosion: 120 (black line), 150 (red line), 200 (green line), and 250 (blue line) days. The location of the atmosphere corresponding to the selected time is shown by dashed lines. The ^{56}Ni mass fraction resulting from explosive nucleosynthesis (Section 3.1) as a function of interior mass is shown by the magenta dashed line.

3.4. Radioactive Tail

Once the photosphere reaches the H/He interface ($t \sim 112$ days), its backward velocity speeds up because of the sudden reduction of the opacity (see above), and it reaches the border of the CO core in roughly 1 day. The penetration of the recombination front in the He core causes a sharp drop in the luminosity because the amount of energy stored in the He core is much less than that present in the H-rich mantle (see the lower two panels in Figure 8). After this sharp drop, the release of energy coming from the stored energy progressively reduces and the luminosity declines, gradually approaching that produced by the ^{56}Co decay (green line in Figure 13). A refined temporal evolution of the luminosity provided by the cascade decay of ^{56}Ni as a function of the amount of ^{56}Ni synthesized in the explosion may be found in Nadyozhin (1994, Equation (19)). In this phase, the light curve is clearly a direct measure of the amount of ^{56}Ni synthesized during the explosion.

It is eventually worth noting that the γ -ray photons released by the radioactive material are not 100% trapped locally, but, as time goes by, a fraction of them are absorbed by more external layers, even outside the formal photosphere. Figure 19 shows the energy deposition function, i.e., the amount of γ -ray photons absorbed by each layer, at various times. Starting from day 200, a fraction of the energy released by ^{56}Co radioactive decay is deposited outside the photosphere (cyan line in Figure 13).

Finally, Figure 13 shows that, in this phase, the total luminosity corresponds to the total instantaneous rate of energy deposition by the radioactive decay of ^{56}Co (magenta line). This is due to the fact that the envelope remains optically thick to the γ -rays until late times. If, on the contrary, the envelope would have become partially thin to them (e.g., because of a lower γ -ray opacity), a fraction of these γ -rays would have freely escaped, and the slope of the light curve would have become steeper.

3.5. The Transition from the Plateau to the Radioactive Tail and the Formation of a Luminosity Bump

We left this part of the temporal evolution of the light curve for the end of this section because it deserves not just a description of what happens but also the presentation of some tests that allow us to identify the physical keys that control the luminosity profile in this phase.

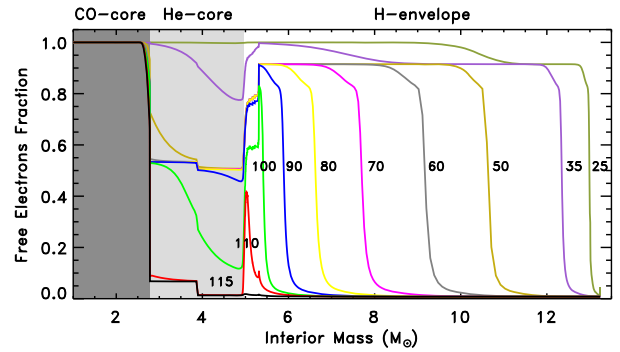


Figure 20. Free electron fraction as a function of interior mass at various times (shown in days close to the various lines). The dark and light gray areas mark the CO and He cores, respectively.

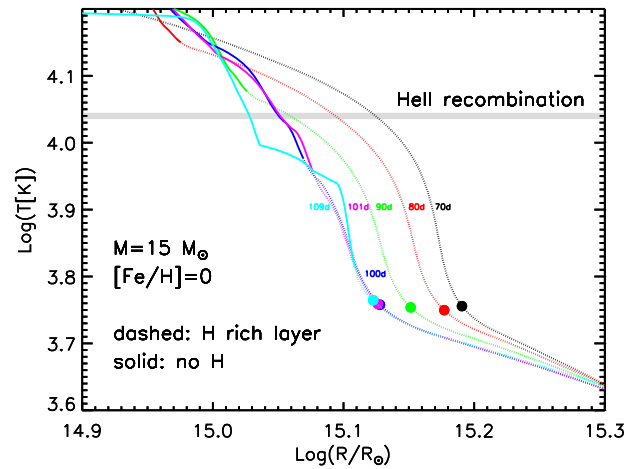


Figure 21. Temperature profile as a function of radius at 70 (black line), 80 (red line), 90 (green line), 100 (blue line), 101 (magenta line), and 109 (cyan line) days, respectively. The dashed part of each line refers to the H-rich matter, while the solid part refers to the region within the He core. The horizontal gray line marks the critical temperature below which He II recombines. The colored dots represent the position of the photosphere.

In addition to the critical temperature that controls the H recombination (~ 5600 K) and hence the position of the photosphere, there is another key temperature: the recombination temperature of He II ($\sim 11,000$ K). This is a crucial temperature because it sharply changes the fraction of free electrons and hence the opacity within the He core. Figure 20 shows the fraction of free electrons at various times. Within the He core (light gray area), He III recombines very early (within the first 50 days or so) when the photosphere is still very far from the H/He discontinuity and reduces the fraction of free electrons from ~ 1 to ~ 0.5 . The He II begins to recombine at roughly day 90, and in 20 days or so, most of the He core is recombined. It is important to note that such a recombination occurs when the photosphere is quite close to the H/He discontinuity. Figures 15 and 16 show very clearly what happens when He II recombines. A low-opacity region begins to form around day 90 in the He core, while on top of it, the H-rich matter is still ionized and hence still has quite a high opacity. Figure 21 shows how the temperature profile changes in time: the dashed part of each line refers to the H-rich matter, while the solid part refers to the region within the He core. The horizontal gray line shows the critical temperature below which He II recombines. The colored dots represent the position of the photosphere. Within the first 100 days or so, the radial

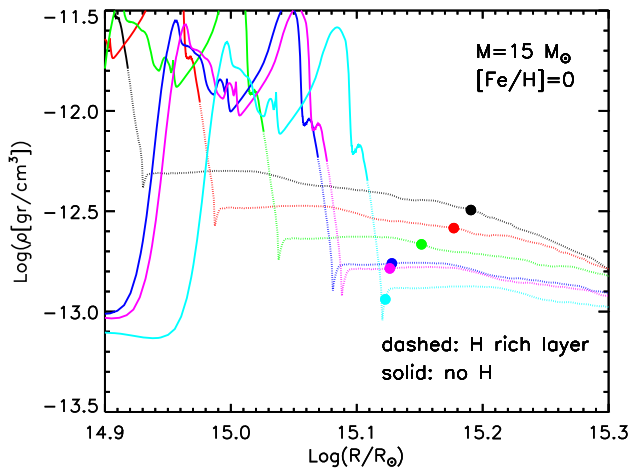


Figure 22. Density profile as a function of the radius at 70 (black line), 80 (red line), 90 (green line), 100 (blue line), 101 (magenta line), and 109 (cyan line) days, respectively. The dashed part of each line refers to the H-rich matter, while the solid part refers to the region within the He core. The colored dots represent the position of the photosphere.

temperature profile preserves its shape (black, red, green, and blue lines in Figure 21). Up to this time, all (or most of) the He core is at temperatures higher than 11,000 K. But between days 100 and 110, He II recombines, the opacity drops down, and a significant fraction of the energy stored in the He core flows outward up to the high-opacity region, where this extra energy is absorbed. Such a sudden injection of energy keeps the temperature of these H-rich layers quite high in spite of the continuous expansion. The blue, magenta, and cyan lines in Figure 21 clearly show that up to day 109 or so, the temperature profile remains roughly constant in the region where $\tau = 2/3$, i.e., in the range $\log(R/R_{\odot}) = 15.10\text{--}15.14$. Only when all of this extra energy is radiated away will the temperature profile start moving inward again, and hence the photosphere as well. Three days later (day 112), the recombination front has moved down to the CO core; since at this point, the energy stored in the He core is too low to maintain the luminosity level of the plateau phase, the light curve bends down, landing on the radioactive tail that dominates the light curve from now on.

The sharp release of energy from the He core explains why the light curve does not bend down when He II recombines, but it does not by itself explain why the luminosity actually increases for a while, creating a bump. We must recall at this point that the temporal evolution of the density does not depend on the temperature or position of the photosphere, since the expansion is homologous in this phase, but rather only depends on the expansion velocity of the various layers. So, in the region of interest, i.e., around $\log(R/R_{\odot}) = 15.10\text{--}15.14$, we are facing a situation in which the density progressively lowers (Figure 22) while the temperature does not. Since τ scales directly with both the opacity and the density ($\tau = \int \kappa \rho dr$), a reduction of the density requires an increase of the opacity to keep the photosphere at $\tau = 2/3$. But the opacity mainly scales with the temperature (only very mildly with the density in these conditions) so that $\tau = 2/3$ requires a higher temperature if the density reduces. In addition to this, the radius of the photosphere slightly increases between days 100 and 109 ($\Delta \log(R) \sim 0.005$). Quantitatively, the luminosity increase at the bump is of the order of $\Delta \log(L) = 0.05$ (by the way,

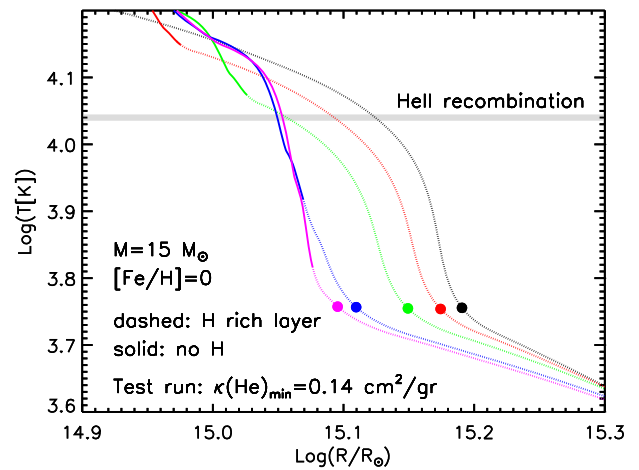


Figure 23. Same as Figure 21 but for the model in which we have artificially inhibited the opacity to decrease below $0.14 \text{ cm}^2 \text{ g}^{-1}$ within the He core.

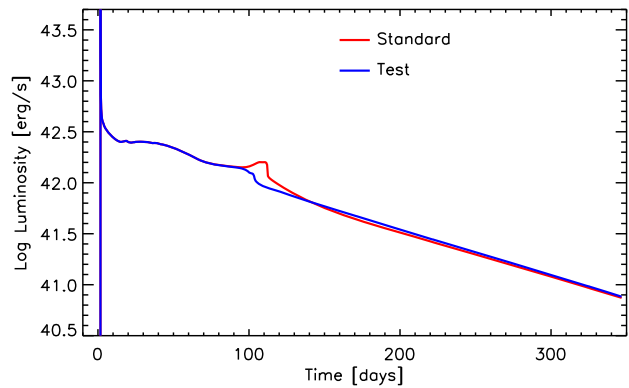


Figure 24. Comparison between the bolometric observed light curve of the standard model (red line) and a test model in which the opacity floor is set artificially to $0.14 \text{ cm}^2 \text{ g}^{-1}$ within the He core (blue line).

a very modest increase), and the temperature of the photosphere increases by $\Delta \log(T_{\text{eff}}) \sim 0.01$. Since $\Delta \log(L) = 2\Delta \log(R) + 4\Delta \log(T_{\text{eff}})$, the temperature increase explains $\sim 80\%$ of the luminosity increase, the remaining $\sim 20\%$ being due to the small increase of the radius of the photosphere.

In order to verify the role played by the opacity drop due to the recombination of He II on the light curve, we have computed a test model in which we have artificially inhibited the opacity to drop below $0.14 \text{ cm}^2 \text{ g}^{-1}$, i.e., the value of the opacity before He II recombination, within the He core. The evolution of the temperature profile of this test run is shown in Figure 23. This figure is analogous to Figure 21. Of course, only after day ~ 90 do the standard and test run start to be different. The most striking difference between Figures 21 and 23 is that now the temperature increase in the region in the range $\log(R/R_{\odot}) = 15.10\text{--}15.14$ is no longer present and the magenta line (in both cases, it refers to day 101) is now free to move leftward, which means that this region can now cool down. So in this case, both the temperature and the density drop down, and the position of the recombination front may recede in radius, forcing the luminosity of the photosphere to decrease. Also in this case, once the photosphere reaches the H/He discontinuity, the luminosity quickly drops until the radioactive tail shows up. Figure 24 shows a comparison between the light curves of the reference and test run. By the

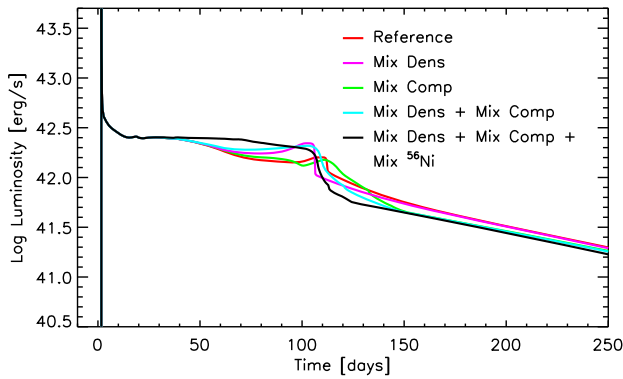


Figure 25. Light curve of the reference model (red line) compared to the ones obtained for various assumptions: the density around the H/He interface is artificially smoothed (magenta line); the chemical composition is artificially mixed, keeping the original density gradient (green line); and both the density and the composition are smoothed (cyan line).

way, note that the high opacity in the He core also produces a slightly shorter plateau.

Though this test clearly confirms our analysis of the reference run, it is obviously an unphysical way to remove the bump. Since, as far as we know, this feature is not observed in the SN IIP light curves, it is important to try to identify which real phenomenon (or phenomena) controls the presence of the bump but also the shape of the light curve while it bends toward the radioactive tail. Utrobin et al. (2017) studied this problem in detail and showed that it generally depends on different factors, e.g., the presence of a density “bump” in the He core, the sharp change of the chemical composition close to the H/He interface, and the spatial distribution of the ⁵⁶Ni produced during the explosion. They concluded that a proper combination of artificial smoothing of the density gradient, the chemical composition at the H/He interface, and the ⁵⁶Ni profile prevents the formation of the luminosity bump in the transition phase from the plateau to the radioactive tail. Such smoothing and mixing should indeed mimic multidimensional effects in spherical symmetry.

We made some tests analogous to those presented by Utrobin et al. (2017) and basically confirmed their finding. Figure 25 summarizes our tests.

In the first test, we artificially smooth the density gradient around the H/He interface $\sim 2 \times 10^6$ s after the explosion. As shown in Figure 26, the density is smoothed between ~ 2.6 and $\sim 9.2 M_{\odot}$. Figure 25 (magenta line) shows that, as was also found by Utrobin et al. (2017), such smoothing implies a shorter plateau and more pronounced bump in the transition phase from the plateau to the radioactive tail compared to the standard model.

In the second test, we keep the original density profile while we artificially smooth the chemical composition, when the elapsed time after the onset of the explosion is 5×10^5 s, by means of “boxcar” averaging (Kasen & Woosley 2009) with a boxcar mass width of $\Delta m = 0.4 M_{\odot}$ (see Figure 27). More specifically, the abundance of each nuclear species k in each zone j is defined as

$$X_{k,j} = \frac{1}{\Delta m} \sum_{i=j}^{j+\Delta m} X_{k,i} \quad j = 1, N, \quad (34)$$

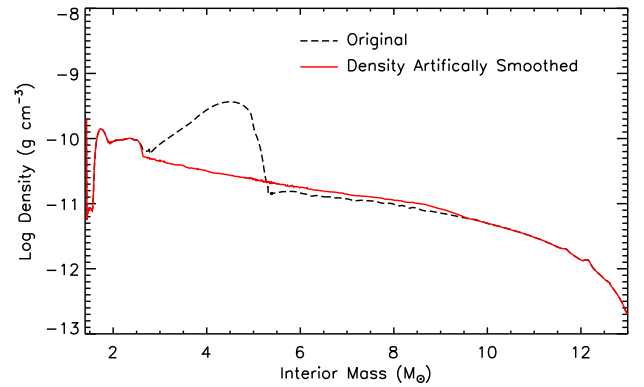


Figure 26. Density profile as a function of interior mass for the reference model $\sim 2 \times 10^6$ s after the onset of the explosion. The black dashed line refers to the original model, while the red solid line refers to the model in which the density is artificially smoothed (see text).

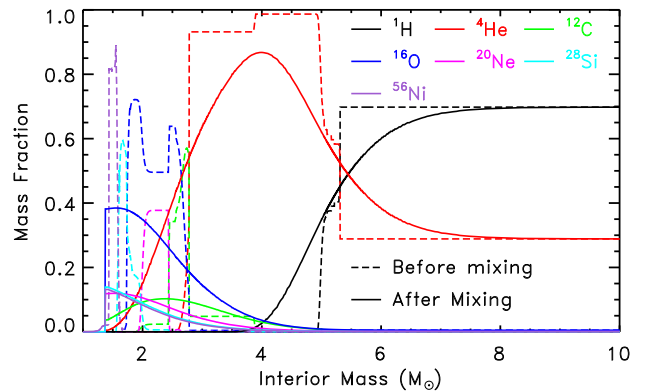


Figure 27. Interior chemical composition of the reference model before and after mixing of chemical composition (see text).

where $j_{\Delta m}$ is the zone such that $m(j_{\Delta m}) - m(j) = \Delta m$ and N is the total number of zones. This calculation is then repeated $n = 4$ times.

In this case, the spike is still present, and the main effect of such mixing is to make the transition between the plateau phase and the radioactive tail smoother (green line in Figure 25). Note that the radioactive tail is slightly less luminous compared to the reference one because of a general decrease of the electron fraction in the ejecta that implies a decrease of the γ -ray opacity ($\kappa_{\gamma} = 0.06 Y_e \text{ cm}^2 \text{ g}^{-1}$).

In the third test, we apply both smoothing of the density and mixing of the composition, as described above. In this case, the two effects discussed in the previous two tests add up to each other (cyan line in Figure 25). In this case, the impact of a difference choice of boxcar mass width is shown in Figure 28. In general, the thicker the boxcar mass, the flatter the plateau and the smoother the transition from the plateau phase to the radioactive tail. Note that in none of these cases have both a flat plateau and a rapid decline of the luminosity from the plateau phase to the radioactive tail been obtained.

The last test is similar to the third test but with additional homogeneous mixing of the ⁵⁶Ni produced during the explosion from the inner edge of the exploding mantle ($1.4 M_{\odot}$) to about half of the H-rich envelope ($9.0 M_{\odot}$). This additional mixing of the ⁵⁶Ni produces an early contribution of the γ -rays to the luminosity, and this implies a flatter plateau, the disappearance of the spike, and a rapid decline of the

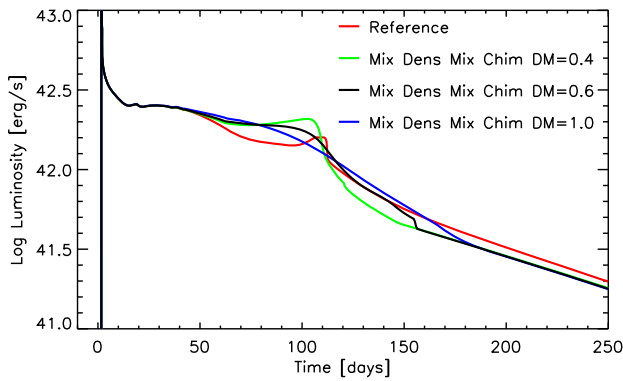


Figure 28. Light curve of the reference model (red line) compared to the ones obtained for various assumptions on the boxcar mass width: $\Delta m = 0.4$ (green line), 0.6 (black line), and 1.0 (blue line).

luminosity in the transition phase from the plateau to the radioactive tail (black line in Figure 25). A similar result was also obtained by Bersten et al. (2011; see their Figure 12). Let us eventually mention that efficient mixing of ^{56}Ni into the H-rich layer is not unreasonable, and it has been confirmed by studies of SN 1987A (Woosley 1988; Arnett 1988; Blinnikov et al. 2000).

As a final comment, let us note that a variation of the outer mass coordinate up to which ^{56}Ni is homogeneously mixed only mildly affects the overall shape of the light curve; i.e., it slightly changes the length of the plateau (Figure 29). Therefore, the choice of this quantity is not crucial in deriving the physical parameters of the progenitor star from the light-curve fitting (see the next section).

4. Explosions and Light Curves of Red Supergiant Models

In the previous section, we described in detail the explosion of a star that may be considered typical, i.e., a nonrotating, solar metallicity $15 M_{\odot}$ model with $E_{\text{expl}} = 1.0$ foe and its associated bolometric light curve.

In this section, we study and discuss how the bolometric light curve depends on the explosion energy. The reason for such a parametric study is that, while in a “real” core-collapse supernova, the energy of the explosion is a natural outcome of the explosion itself (and uniquely determined by the initial mass, metallicity, and, eventually, initial rotational velocity of the progenitor star), our modeling of the explosion requires the injection of some arbitrary amount of energy to generate the shock wave (like the vast majority of similar computations available in the literature; see Section 3). This is the reason we are forced to compute a grid of simulations for different (arbitrary) amounts of explosion energies that in most cases lead to results that do not correspond to more sophisticated multidimensional explosions or to the typical observed values.

Since we are focusing on the bolometric light curves of the SNe IIP, we only computed the explosions of the subset of models present in our database published in Limongi & Chieffi (2018) that reach core collapse as red supergiant stars.

The main properties of these models, relevant for the light-curve calculations, are reported in Table 2: model identifier (column 1), initial mass (column 2), initial metallicity (column 3), effective temperature (column 4), luminosity (column 5), mass at the time of the explosion (column 6), mass of the He core (column 7), mass of the CO core (column 8), mass of the

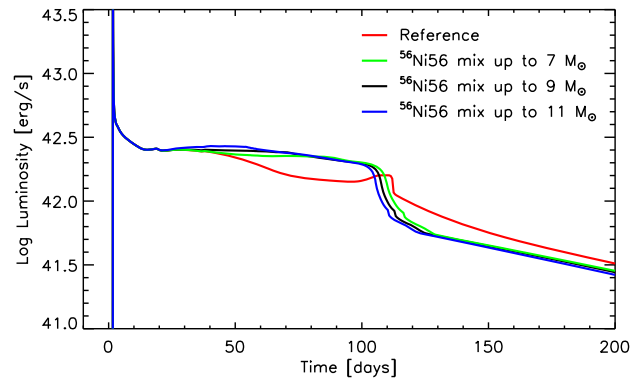


Figure 29. Light curve of the reference model (red line) compared to the ones obtained for various assumptions on the outermost mass coordinate up to which the ^{56}Ni is homogeneously mixed.

Fe core (column 9), amount of H and He in the envelope (columns 10 and 11, respectively), binding energy of the material outside the Fe core (column 12), mass of the H envelope (defined as the difference between the total mass and the mass coordinate where the H mass fraction drops below 10^{-4}) in units of $10 M_{\odot}$ (column 13), and total radius in units of $500 R_{\odot}$ (column 14).

For each presupernova progenitor (reported in Table 2), we computed a grid of different explosions for various explosion energies. All of the explosions were computed by assuming a smoothing density profile, as well as a mixing of the chemical composition and ^{56}Ni as described in the previous paragraph. In particular, ^{56}Ni is always mixed from the base of the ejecta, after the shock breakout and fallback are ended, up to half of the H-rich envelope. As Figure 29 shows, this choice does not significantly affect the shape of the light curve in the late stages of the plateau and in the transition between the plateau and the radioactive tail.

The main results of these calculations are reported in Table 3: model identifier (column 1); explosion energy (column 2; mainly the kinetic energy of the ejecta); time elapsed at the shock breakout (column 3); time to the end of the fallback of material onto the remnant (column 4); amount of ^{56}Ni ejected (column 5); mass of the remnant, including the fallback material (column 6); mass of the ejecta (column 7); bolometric luminosities 30 and 50 days after the shock breakout (columns 8 and 9, respectively); and time duration of the plateau phase, in days, assuming that the beginning of the plateau coincides with the shock breakout and defining the end of the plateau when the radius of the photosphere reduces to 50% of its maximum value (column 10).

Figures 30–34 show the light curves obtained for some selected progenitor models as a function of the explosion energy.

These figures visually show how the shape of the light curve depends on the progenitor mass, initial metallicity, and explosion energy. In general, for the same progenitor star, an increase of the explosion energy implies an increase of the luminosity of the plateau, a decrease of its duration (in time), a decrease of the remnant mass, and an increase of ^{56}Ni ejected. It goes without saying that the radioactive tail in the light curve disappears if the amount of ^{56}Ni ejected is negligible (see the legends in Figures 30–34).

Figure 35 shows the remnant mass (on the primary y-axis) and the ^{56}Ni ejected (on the secondary y-axis) as a function of

Table 2
Properties of the Presupernova Models

Model ID	M_i (M_\odot)	[Fe/H]	$\log(T_{\text{eff}})$ (K)	$\log(L/L_\odot)$	M_f (M_\odot)	M_{He} (M_\odot)	M_{CO} (M_\odot)	M_{Fe} (M_\odot)	H (M_\odot)	He (M_\odot)	E_{bind} (10^{51} erg)	M_{10} ($10 M_\odot$)	R_{500} ($500 R_\odot$)
(1)	(2)	(3)	(4)	(5)	(6)	(7)	(8)	(9)	(10)	(11)	(12)	(13)	(14)
13a	13	0	3.55	4.82	11.9	4.08	2.03	1.36	5.37	4.31	0.65	0.784	1.324
15a	15	0	3.54	4.98	13.3	4.95	2.78	1.43	5.67	4.63	0.95	0.833	1.678
13b	13	-1	3.60	4.85	12.5	4.26	2.13	1.19	5.83	4.44	1.08	0.826	1.125
15b	15	-1	3.59	5.05	14.2	5.22	3.01	1.40	6.34	4.54	1.33	0.900	1.477
20b	20	-1	3.59	5.26	18.4	7.52	4.21	1.43	7.47	6.50	1.79	1.090	1.862
25b	25	-1	3.58	5.48	20.6	10.20	6.82	1.59	6.96	6.62	4.02	1.049	2.521
13c	13	-2	3.65	4.88	13.0	4.34	2.14	1.40	6.23	4.44	0.85	0.866	0.935
15c	15	-2	3.64	5.01	14.8	5.21	2.72	1.08	6.86	5.09	1.70	0.964	1.092
20c	20	-2	3.64	5.27	19.7	7.49	4.23	1.43	8.60	6.71	1.83	1.230	1.483
25c	25	-2	3.67	5.20	24.7	9.87	5.93	1.53	10.20	8.26	2.54	1.490	1.220
13d	13	-3	3.66	4.88	13.0	4.22	2.15	1.15	6.22	4.44	1.30	0.878	0.857
15d	15	-3	3.66	5.06	15.0	5.22	3.09	1.46	6.95	4.62	1.45	0.981	1.082
20d	20	-3	3.66	5.26	19.8	7.42	4.35	1.44	8.64	6.63	1.86	1.252	1.358
25d	25	-3	3.66	5.46	24.6	9.84	6.29	1.53	10.13	8.00	2.89	1.495	1.709

the explosion energy for the various progenitor masses for each initial metallicity. In general, for any initial metallicity, the remnant mass scales inversely with the explosion energy and directly with the progenitor mass. The obvious reason for this behavior is that the larger the initial mass, the larger the binding energy of the mantle of the star above the iron core (Table 2). As the metallicity decreases, the dramatic reduction of the mass loss implies larger CO cores for the same initial mass and therefore a higher binding energy. Therefore, at lower metallicities, more massive remnants are obtained for the same progenitor mass and explosion energies. As discussed in Section 4, the amount of ^{56}Ni ejected depends on the remnant mass. In general, the larger the remnant mass, the smaller the ^{56}Ni ejected. For progenitor masses smaller than $20 M_\odot$, a sizable amount of ^{56}Ni is ejected only for explosion energies larger than ~ 0.5 foe. In particular, the amount of ^{56}Ni increases rapidly for explosion energies in the range ~ 0.5 – 1.0 foe, and then it remains almost constant for larger explosion energies. For progenitor stars with an initial mass of $\sim 20 M_\odot$, a substantial amount of ^{56}Ni is ejected only for explosion energies larger ~ 1.5 foe. For more massive progenitors, no ^{56}Ni is ejected in this range of explosion energies. As a final comment, let us note that the fallback occurs on rather long timescales, ranging from a few dozen up to $\sim 10^6$ – 10^7 s (see Table 3), and that in general, the lower the explosion energy, the longer the duration of the fallback.

As we have shown in Section 4, the luminosity of the plateau at late stages depends, among other things, on the mixing of ^{56}Ni . Therefore, the average luminosity of the plateau must be evaluated at early times if we want it to be unaffected by the amount of ^{56}Ni ejected. For this reason, we choose to define the average luminosity of the plateau as the luminosity at ~ 30 days after the shock breakout (L_{30}), rather than the one evaluated after 50 days (L_{50} ; Kasen & Woosley 2009; Sukhbold et al. 2016). Figure 36 shows this quantity (L_{30}) as a function of explosion energy for the various progenitor stars and initial metallicities. Overall, $\log L_{30}$ varies between ~ 41.6 and ~ 42.7 , i.e., slightly more than 1 order of magnitude. In general, for any initial metallicity, L_{30} increases significantly with the explosion energy. The reason is that the luminosity scales with $\sim R^2 T^4$,

where both R and T are evaluated at the photosphere; the temperature is roughly constant, since it corresponds to that for the H recombination (see Figure 16), while R scales directly with the kinetic energy of the ejecta that dominates the explosion energy. This last occurrence is due to the fact that, in order to obtain a higher final kinetic energy of the ejecta for any given progenitor mass, a larger amount of energy must be injected to start the explosion. Since, as discussed in Section 4 (see also Figure 8), the internal energy in the H-rich mantle at the time of the shock breakout is about half of the total energy (the remaining being the kinetic energy), the higher the amount of energy injected to start the explosion, the higher the internal energy in the envelope at the beginning of the adiabatic cooling (see Section 3.2). Since, as mentioned in Section 3.2, during adiabatic cooling the radius scales as $R \propto 1/T$, in more energetic explosions the envelope will have to expand more (starting from a higher internal energy content) to reach the radius corresponding to the H recombination temperature.

For a similar reason, in general, L_{30} also increases slightly with the progenitor mass for the same explosion energy. First, the amount of energy to be injected in a star to obtain the same final kinetic energy of the ejecta scales directly with the progenitor mass (actually the He core mass); second, the radius of a star at the onset of the collapse scales directly with the initial mass (obviously, we are considering only red supergiant stars here).

The dependence of L_{30} on the initial metallicity can be appreciated in Figure 37, where L_{30} is shown as a function of explosion energy for the various metallicities for each progenitor mass. As expected, for a fixed explosion energy, L_{30} decreases with decreasing the initial metallicity because lower-metallicity stars are generally more compact than the higher-metallicity ones. This effect, however, is modest for lower-mass models and increases slightly for the more massive ones.

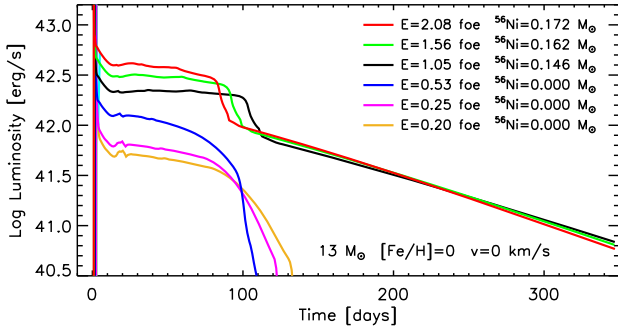
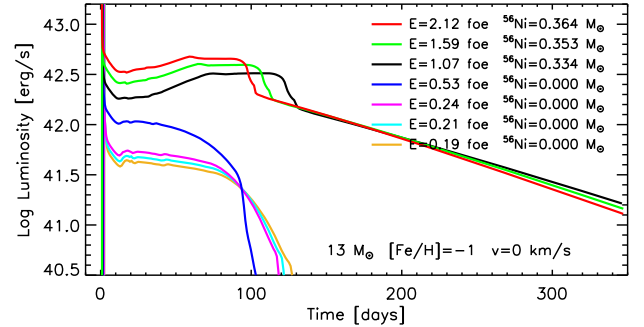
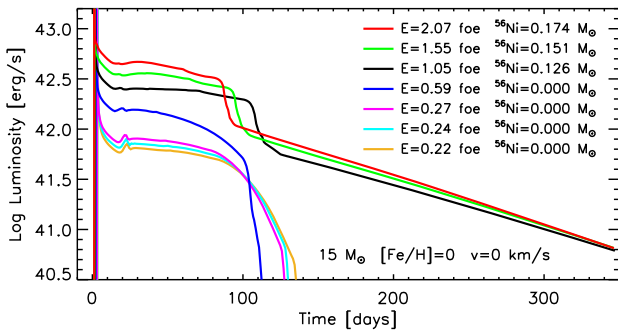
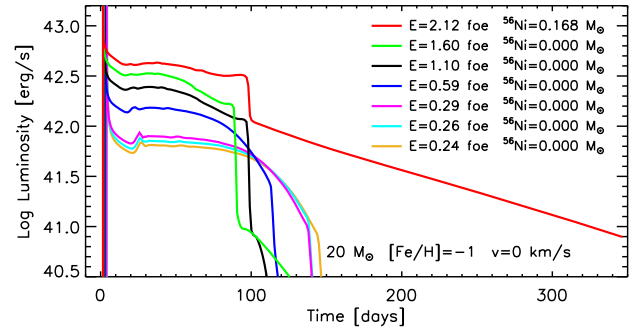
As already discussed in Sections 3.3 and 3.4, the plateau phase ends when the photosphere approaches the He core. In general, the time at which the photosphere reaches the H/He interface decreases with increasing the expansion velocity and therefore with the explosion energy (Figure 38). As a

Table 3
Main Results of the Explosion Calculations

Model ID (1)	E_{expl} (erg) (2)	t_{breakout} (s) (3)	t_{fallback} (s) (4)	$^{56}\text{Ni}_{\text{ejected}}$ (M_{\odot}) (5)	M_{rem} (M_{\odot}) (6)	M_{ejecta} (M_{\odot}) (7)	$\log(L_{30})$ (erg s $^{-1}$) (8)	$\log(L_{50})$ (erg s $^{-1}$) (9)	t_{plateau} (days) (10)
13a	1.99E+50	2.35E+05	2.92E+07	9.78E-40	2.15	9.71	41.703	41.658	1.27E+02
13a	2.50E+50	2.11E+05	1.73E+07	9.84E-40	2.03	9.83	41.796	41.752	1.17E+02
13a	5.34E+50	1.49E+05	1.29E+06	7.48E-05	1.60	10.26	42.087	42.018	1.07E+02
13a	1.05E+51	1.12E+05	1.21E+02	1.46E-01	0.86	11.00	42.342	42.339	1.12E+02
13a	1.56E+51	9.16E+04	7.79E+01	1.62E-01	0.84	11.02	42.502	42.478	9.93E+01
13a	2.08E+51	8.02E+04	0.00E+00	1.72E-01	0.81	11.05	42.606	42.576	9.08E+01
15a	2.17E+50	2.92E+05	1.79E+07	1.03E-39	3.00	10.23	41.808	41.789	1.30E+02
15a	2.43E+50	2.78E+05	1.53E+07	1.04E-39	2.89	10.35	41.853	41.833	1.27E+02
15a	2.74E+50	2.61E+05	2.55E+07	1.05E-39	2.89	10.34	41.905	41.880	1.23E+02
15a	5.88E+50	1.87E+05	1.62E+05	6.33E-17	2.14	11.09	42.192	42.141	1.12E+02
15a	1.05E+51	1.45E+05	1.07E+04	1.26E-01	1.41	11.82	42.403	42.395	1.15E+02
15a	1.55E+51	1.21E+05	2.22E+02	1.51E-01	0.89	12.35	42.555	42.534	9.99E+01
15a	2.07E+51	1.06E+05	1.51E+02	1.74E-01	0.85	12.38	42.670	42.624	9.13E+01
13b	1.88E+50	2.11E+05	2.19E+07	1.02E-39	2.32	10.17	41.621	41.588	1.17E+02
13b	2.12E+50	2.00E+05	2.25E+07	1.03E-39	2.25	10.24	41.668	41.634	1.14E+02
13b	2.41E+50	1.87E+05	1.75E+07	1.03E-39	2.22	10.26	41.722	41.683	1.12E+02
13b	5.29E+50	1.31E+05	1.59E+06	3.91E-13	1.76	10.73	42.020	41.960	1.04E+02
13b	1.07E+51	9.79E+04	3.17E+02	3.34E-01	0.85	11.63	42.278	42.389	1.31E+02
13b	1.59E+51	8.04E+04	5.93E+01	3.53E-01	0.83	11.66	42.446	42.534	1.14E+02
13b	2.12E+51	6.98E+04	0.00E+00	3.64E-01	0.81	11.68	42.567	42.637	1.03E+02
15b	2.19E+50	2.63E+05	2.27E+07	1.08E-39	3.46	10.71	41.762	41.749	1.33E+02
15b	2.44E+50	2.50E+05	1.95E+07	1.09E-39	3.46	10.71	41.805	41.789	1.23E+02
15b	5.91E+50	1.68E+05	1.93E+05	1.36E-23	2.47	11.71	42.146	42.102	1.17E+02
15b	1.06E+51	1.31E+05	2.80E+04	2.59E-02	1.60	12.58	42.358	42.316	1.00E+02
15b	1.56E+51	1.10E+05	2.03E+04	2.07E-01	1.33	12.85	42.511	42.516	1.15E+02
15b	2.08E+51	9.71E+04	7.93E+05	2.31E-01	1.31	13.28	42.625	42.672	8.75E+01
20b	2.35E+50	3.62E+05	4.26E+06	1.34E-39	5.02	13.34	41.804	41.801	1.40E+02
20b	2.63E+50	3.46E+05	4.17E+05	1.35E-39	4.87	13.48	41.845	41.845	1.38E+02
20b	2.90E+50	3.27E+05	6.51E+06	1.36E-39	4.83	13.52	41.894	41.897	1.36E+02
20b	5.93E+50	2.36E+05	9.30E+06	1.44E-39	4.01	14.34	42.182	42.163	1.15E+02
20b	1.10E+51	1.83E+05	2.13E+05	2.67E-17	2.53	15.83	42.390	42.348	1.06E+02
20b	1.60E+51	1.54E+05	2.21E+05	5.69E-09	1.95	16.41	42.525	42.474	9.17E+01
20b	2.12E+51	1.37E+05	3.83E+04	1.68E-01	1.57	16.79	42.628	42.606	9.92E+01
25b	4.39E+50	3.59E+05	1.99E+05	1.31E-39	7.54	13.04	42.143	42.189	1.26E+02
25b	1.15E+51	2.36E+05	1.68E+06	4.32E-19	5.67	14.91	42.513	42.515	1.04E+02
25b	1.62E+51	2.05E+05	1.36E+05	2.99E-18	4.04	16.54	42.635	42.622	9.49E+01
25b	2.12E+51	1.85E+05	1.09E+07	5.71E-12	3.24	17.34	42.726	42.708	8.42E+01
13c	2.37E+50	1.59E+05	2.82E+07	1.06E-39	2.39	10.57	41.639	41.606	1.08E+02
13c	5.62E+50	1.07E+05	9.29E+05	1.58E-13	1.94	11.03	41.974	41.916	9.65E+01
13c	1.06E+51	8.23E+04	1.84E+02	2.28E-01	0.90	12.07	42.202	42.292	1.24E+02
13c	1.59E+51	6.84E+04	1.66E+02	2.52E-01	0.85	12.11	42.381	42.449	1.08E+02
13c	2.11E+51	5.93E+04	6.46E+01	2.70E-01	0.84	12.13	42.491	42.552	9.87E+01
15c	2.02E+50	2.12E+05	1.31E+07	1.17E-39	3.17	11.62	41.601	41.578	1.18E+02
15c	2.28E+50	1.99E+05	1.89E+07	1.18E-39	3.07	11.72	41.650	41.625	1.15E+02
15c	5.69E+50	1.32E+05	5.91E+05	9.05E-25	2.50	12.29	42.011	41.959	1.02E+02
15c	1.09E+51	1.01E+05	1.88E+05	4.09E-01	0.98	13.81	42.228	42.331	1.49E+02
15c	1.61E+51	8.47E+04	1.60E+02	4.42E-01	0.87	13.92	42.383	42.499	1.27E+02
15c	2.14E+51	7.37E+04	2.39E+01	4.69E-01	0.84	13.95	42.504	42.612	1.16E+02
20c	2.33E+50	3.01E+05	2.92E+07	1.47E-39	5.27	14.46	41.700	41.703	1.38E+02
20c	2.61E+50	2.87E+05	7.84E+06	1.48E-39	4.99	14.73	41.744	41.739	1.35E+02
20c	5.94E+50	1.96E+05	1.53E+07	1.57E-39	4.08	15.64	42.085	42.058	1.17E+02
20c	1.09E+51	1.53E+05	5.12E+05	3.67E-16	2.58	17.14	42.293	42.248	1.02E+02
20c	1.59E+51	1.28E+05	3.00E+05	1.14E-11	1.99	17.74	42.428	42.377	9.14E+01
20c	2.12E+51	1.13E+05	2.67E+04	1.76E-01	1.58	18.14	42.531	42.511	1.04E+02

Table 3
(Continued)

Model ID	E_{expl} (erg)	t_{breakout} (s)	t_{fallback} (s)	$^{56}\text{Ni}_{\text{ejected}}$ (M_{\odot})	M_{rem} (M_{\odot})	M_{ejecta} (M_{\odot})	$\log(L_{30})$ (erg s^{-1})	$\log(L_{50})$ (erg s^{-1})	t_{plateau} (days)
(1)	(2)	(3)	(4)	(5)	(6)	(7)	(8)	(9)	(10)
25c	2.38E+50	2.48E+05	7.03E+06	1.74E-39	7.42	17.23	41.680	41.593	1.30E+02
25c	2.66E+50	2.35E+05	2.15E+05	1.75E-39	7.22	17.44	41.717	41.629	1.29E+02
25c	2.98E+50	2.21E+05	5.30E+05	1.77E-39	7.03	17.62	41.762	41.668	1.27E+02
25c	1.08E+51	1.29E+05	9.02E+04	1.73E-16	4.17	20.48	42.198	42.048	9.20E+01
25c	1.58E+51	1.09E+05	3.97E+05	3.96E-16	2.86	21.80	42.320	42.148	8.21E+01
25c	2.08E+51	9.60E+04	1.96E+05	1.68E-11	2.38	22.28	42.408	42.214	5.06E+01
13d	2.17E+50	1.52E+05	2.81E+07	1.06E-39	2.44	10.54	41.571	41.538	1.06E+02
13d	5.38E+50	9.99E+04	2.76E+06	5.64E-14	1.90	11.07	41.924	41.861	1.00E+02
13d	1.07E+51	7.64E+04	1.63E+02	3.77E-01	0.86	12.12	42.187	42.342	1.37E+02
13d	1.60E+51	6.28E+04	4.07E+01	4.04E-01	0.83	12.15	42.359	42.501	1.21E+02
15d	2.95E+50	1.73E+05	1.84E+07	1.16E-39	3.51	11.44	41.763	41.735	1.14E+02
15d	6.05E+50	1.25E+05	1.07E+05	6.52E-17	2.70	12.25	42.033	41.987	1.16E+02
15d	1.07E+51	9.81E+04	3.10E+04	2.61E-02	1.70	13.25	42.237	42.201	1.03E+02
15d	2.10E+51	7.31E+04	9.60E+02	2.73E-01	0.87	14.08	42.500	42.542	1.07E+02
20d	6.18E+50	1.80E+05	2.25E+05	1.58E-39	4.03	15.76	42.054	42.018	1.14E+02
20d	1.10E+51	1.40E+05	2.61E+05	2.36E-16	2.57	17.22	42.261	42.210	1.04E+02
20d	1.59E+51	1.19E+05	1.58E+05	9.96E-10	2.03	17.76	42.398	42.340	8.87E+01
20d	2.12E+51	1.04E+05	2.89E+04	2.14E-01	1.56	18.23	42.501	42.484	5.04E+01
25d	1.09E+51	1.90E+05	1.87E+07	1.90E-16	4.65	19.98	42.298	42.273	1.17E+02
25d	1.59E+51	1.62E+05	7.22E+04	5.16E-16	3.13	21.50	42.429	42.404	1.03E+02
25d	2.11E+51	1.44E+05	2.19E+05	6.72E-12	2.55	22.08	42.531	42.500	9.50E+01


Figure 30. Bolometric light curves of a nonrotating, solar metallicity $13 M_{\odot}$ for different explosion energies. The ^{56}Ni shown in the legend is the one produced during the explosion. In each case, we assume a smoothing of the density, a mixing of the chemical composition, and ^{56}Ni as described in the text.

Figure 32. Same as Figure 30 but for a nonrotating, $13 M_{\odot}$ with initial composition corresponding to $[\text{Fe}/\text{H}] = -1$ (see text).

Figure 31. Same as Figure 30 but for a nonrotating, solar metallicity $15 M_{\odot}$.

Figure 33. Same as Figure 30 but for a nonrotating, $20 M_{\odot}$ with initial composition corresponding to $[\text{Fe}/\text{H}] = -1$ (see text).

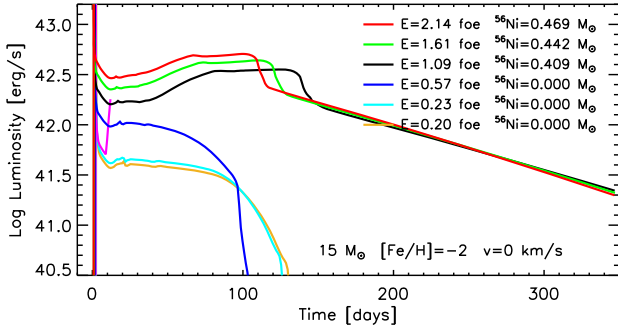


Figure 34. Same as Figure 30 but for a nonrotating, $15 M_{\odot}$ with initial composition corresponding to $[\text{Fe}/\text{H}] = -2$ (see text).

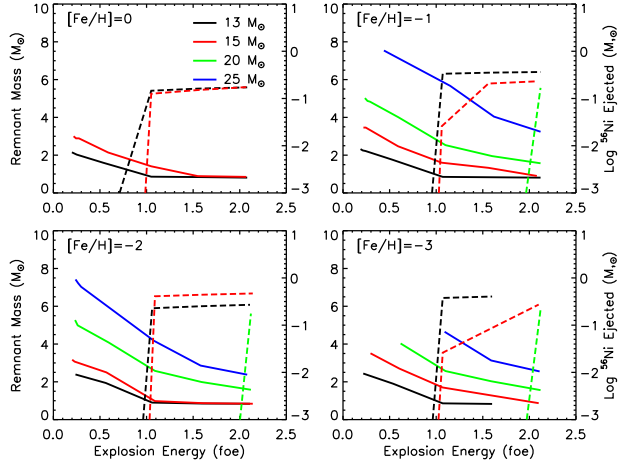


Figure 35. Remnant mass (primary y-axis) and ^{56}Ni ejected (secondary y-axis) as a function of explosion energy for the various progenitor masses (see colors in the legend) and initial metallicities: $[\text{Fe}/\text{H}] = 0$ (upper left panel), -1 (upper right panel), -2 (lower left panel), and -3 (lower right panel).

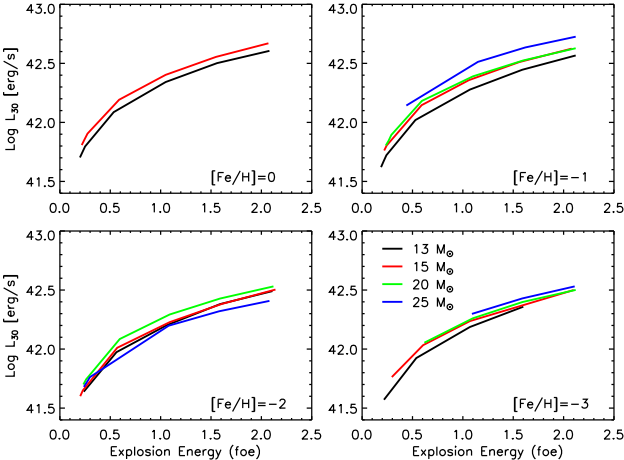


Figure 36. Luminosity at ~ 30 days after the shock breakout (L_{30}) as a function of explosion energy for the various progenitor masses (see colors in the legend) and initial metallicities: $[\text{Fe}/\text{H}] = 0$ (upper left panel), -1 (upper right panel), -2 (lower left panel), and -3 (lower right panel).

consequence, the duration of the plateau decreases with increasing the explosion energy. However, since this quantity also depends on the amount of ^{56}Ni ejected and the mass of the

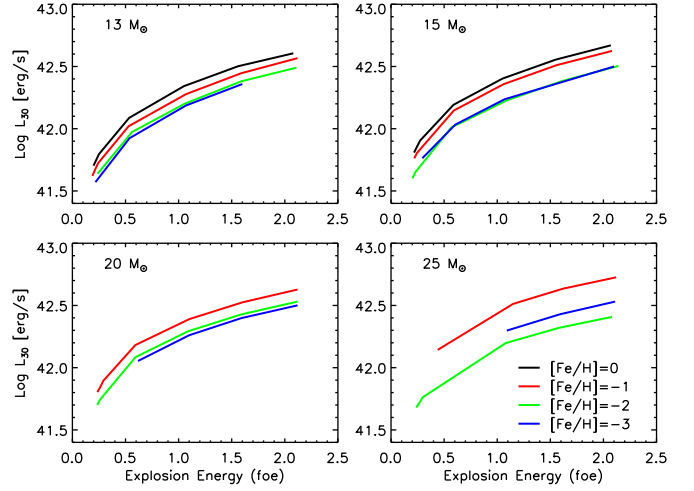


Figure 37. Luminosity at ~ 30 days after the shock breakout (L_{30}) as a function of explosion energy for the various metallicities (see colors in the legend) and progenitor masses: $13 M_{\odot}$ (upper left panel), $15 M_{\odot}$ (upper right panel), $20 M_{\odot}$ (lower left panel), and $13 M_{\odot}$ (lower right panel).

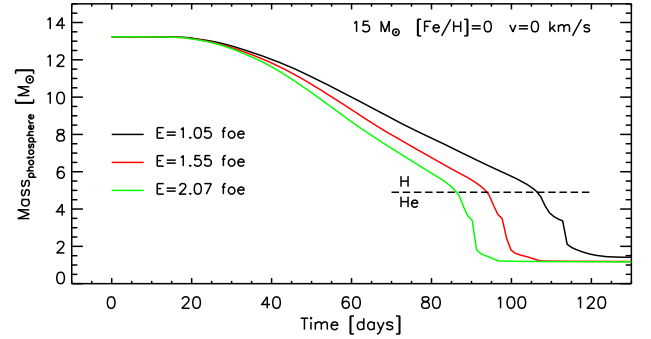


Figure 38. Location in the mass of the photosphere as a function of time for model 15a for various explosion energies (see color legend). The horizontal black dashed line marks the H/He interface.

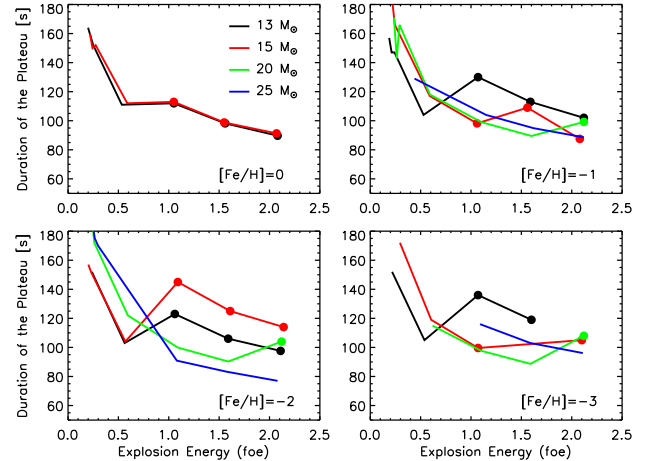


Figure 39. Plateau duration as a function of explosion energy for the various progenitor masses and initial metallicities. The colored dots mark the cases where enough ^{56}Ni is ejected (see Table 3). The plateau duration is defined when the radius of the photosphere decreases down to 50% of its maximum value.

H-rich envelope, the trend is not monotonic over the whole range of explosion energies, progenitor masses, and initial metallicities. In particular, Figure 39 shows the existence of

two distinct behaviors as a function of explosion energy, depending on the amount of ^{56}Ni ejected. The plateau duration initially decreases as the explosion energy increases as long as the amount of ^{56}Ni ejected is lower than $\sim 10^{-3} M_{\odot}$. When this quantity increases enough, the plateau duration starts increasing until it reaches a local maximum and then decreases again for higher explosion energies. Note that in all models where the ^{56}Ni ejected is negligible, the plateau duration decreases monotonically with an increase in the explosion energy.

5. Comparison with Observations

As a first application of the simulations discussed in the previous sections, we applied this database of explosions to derive the physical properties of the progenitor of the well-known SN II SN 1999em. A detailed and more extended study of a larger sample of supernovae will be presented in a subsequent paper. We have chosen SN 1999em because it is a widely studied supernova, its bolometric light curve is available in the literature, and there are high-quality optical images of its host galaxy before its explosion (Elmhamdi et al. 2003; Smartt et al. 2002; Sohn & Davidge 1998).

On 1999 October 29, SN 1999em was discovered by the Lick Observatory Supernova Search in NGC 1637 (Li 1999) at an unfiltered CCD magnitude of ~ 13.5 mag. It was soon confirmed as an SN II, and, since it was a bright event, it has been well studied both spectroscopically and photometrically for more than 500 days (Hamuy et al. 2001; Leonard 2002; Elmhamdi et al. 2003). It has been classified as a normal SN IIP due to the long plateau phase lasting ~ 90 days (Leonard et al. 2001). Observations in radio and X-ray wavelengths at early times provided information on the structure of the circumstellar material and are consistent with a mass-loss rate of $\sim 2 \times 10^{-6} M_{\odot} \text{ yr}^{-1}$ and a wind velocity of $\sim 10 \text{ km s}^{-1}$ (Pooley et al. 2001), i.e., consistent with a red supergiant progenitor. The nature of the progenitor was discussed by Smartt et al. (2002), who used high-resolution optical images of NGC 1637 taken several years before the SN 1999em event by Sohn & Davidge (1998) at the Canada–France–Hawaii Telescope (CFHT). In particular, due to the lack of point sources at the position corresponding to SN 1999em, they derived bolometric luminosity limits and constrained the luminosity of the progenitor star as a function of the assumed effective temperature (see their Figure 4).

The determination of the distance is obviously fundamental to comparing the theoretical light curve with the observed one. Unfortunately, there is no agreement on this point. Using the expanding photospheric method (EPM; Kirshner & Kwan 1974), the following values have been obtained: 7.5 ± 0.1 (Hamuy et al. 2001), 8.2 ± 0.6 (Leonard 2002), and 7.83 ± 0.3 (Elmhamdi et al. 2003) Mpc. On the other hand Leonard et al. (2003) identified 41 Cepheid variable stars in NGC 1637, the host galaxy of SN 1999em, and derived a Cepheid distance to this galaxy of 11.7 ± 1.0 Mpc, which is $\sim 50\%$ higher than the one derived with the EPM. Sohn & Davidge (1998) studied the bright stellar content in NGC 1637 and estimated a distance of 7.8 ± 1.0 Mpc using the brightest red supergiant method, a value close to the one obtained with the EPM. On the other hand, Baron et al. (2004) obtained a distance to SN 1999em of 12.5 ± 1.8 Mpc by means of the spectral-fitting expanding atmospheric model (SEAM), a value in agreement with the Cepheid distance obtained by Leonard et al. (2003). Dessart & Hillier (2006), improving the EPM,

found a value of 11.5 ± 1.0 Mpc, which is consistent with the SEAM and Cepheid distances.

Since the distance to SN 1999em is still under debate, we present a comparison between the observed and theoretical bolometric light curves for the two extreme values of the distance reported in the literature. In particular, we will consider the bolometric light curve based on the photometry of Elmhamdi et al. (2003), Leonard et al. (2001), Hamuy et al. (2001), Leonard et al. (2003) S. Benetti, private communication) for the two different adopted distances, i.e., 7.83 (LD) and 11.7 (HD) Mpc. In both cases, the total extinction adopted is $A_V = 0.31$.

In general, the comparison between the observations and the models proceeds through the following steps. First, we select the models among those reported in Table 3 with a metallicity similar to that of the SN host galaxy. Second, we consider only those for which L_{30} is close to the observed one. Third, we modify the ejected ^{56}Ni and rerun the simulation in order to fit the radioactive tail. Finally, we fit the shape of the light curve in the transition phase between the plateau and the radioactive tail by changing the efficiency and the extension of the mixing of both the chemical composition and the ^{56}Ni (also in this case, this final step requires additional simulations).

It is worth noting that, in general, the database of light curves reported in Table 3 cannot be used *sic et simpliciter*, but they must be complemented by additional simulations in order to really constrain the fit of the SN light curve under examination (L_{30} , ^{56}Ni , and the shape of the transition phase between the plateau and the radioactive tail). Hence, the calculations reported in Table 3 must be seen as a basic database useful to study the general dependence of the light curves on the initial progenitor parameters (mass and metallicity) and the features of the explosion itself.

Let us also stress that, if we know only the metallicity of the host galaxy and the bolometric light curve of a given supernova, we cannot disentangle the progenitor mass and kinetic energy of the ejecta. In fact, for a given metallicity, we can obtain the same value of $\log L_{30}$ by changing both the progenitor mass and the kinetic energy of the ejecta (see Figure 36). Only independent knowledge of one of the two would fix the other.

Having said this, let us turn to the fit to SN 1999em. According to the relation between the absolute magnitude and the metallicity for external galaxies (Brodie & Huchra 1991), Sohn & Davidge (1998) derived a metallicity of $[\text{Fe}/\text{H}] \sim -0.33$ for NGC 1637. Since this metallicity falls between the two grid points, i.e., $[\text{Fe}/\text{H}] = 0$ and -1 , we consider these two sets of models.

In the LD case, the observed $\log L_{30}$ is ~ 41.7 ; therefore, from Figure 36 and Table 3, we select models 13a, with $E_{\text{expl}} = 1.99 \times 10^{50}$ erg (hereafter 13a1), and 13b, with $E_{\text{expl}} = 2.41 \times 10^{50}$ erg (hereafter 13b3). For all other computed models, $\log L_{30}$ is larger than the observed value. Therefore, both of these progenitor masses and explosion energies should be considered as upper limits (see Figure 36).

Let us start by analyzing model 13b3. Figure 40 shows the comparison between the observations (blue dots) and the light curve of the model (black line). While the L_{30} is in good agreement with the observed one, the model does not show a radioactive tail because of the large remnant mass ($M_{\text{rem}} = 2.22 M_{\odot}$; see Table 3) that implies a negligible amount of ^{56}Ni ejected. For this reason, we assume that some

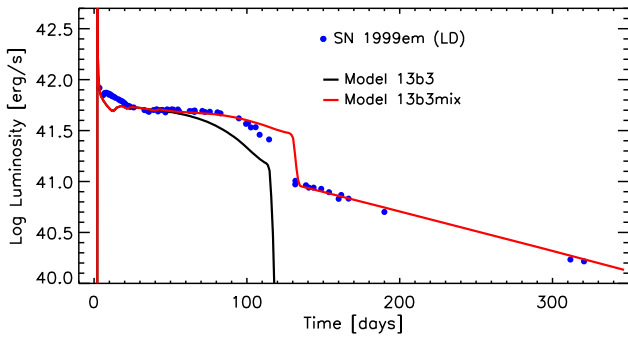


Figure 40. Light curve of models 13b3 (black line) and 13b3mix (red line) in which $\sim 0.022 M_{\odot}$ of ^{56}Ni is deposited and homogeneously mixed up to a mass coordinate marking half of the H-rich envelope. The blue dots refer to the observed bolometric light curve in the LD case (see text).

amount of ^{56}Ni is mixed from the innermost zones outward in mass during the explosion, before the occurrence of the fallback, and we simulate such a phenomenon simply by depositing and homogeneously mixing the amount of ^{56}Ni required to fit the radioactive tail. We perform such ^{56}Ni deposition and homogeneous mixing soon after (~ 10 days) the shock breakout. It is important to note at this point that the ^{56}Ni synthesized in the innermost zones before the occurrence of the fallback is much higher than $\sim 0.022 M_{\odot}$, and therefore it is reasonable to assume that a small fraction of such ^{56}Ni can be mixed upward in mass before the fallback goes to completion. By the way, let us recall that the outer edge of the zone where the ^{56}Ni is homogeneously mixed corresponds to the mass coordinate marking half of the H-rich envelope. Figure 40 shows that the light curve of the model (red line) in which $\sim 0.022 M_{\odot}$ is deposited and homogeneously mixed (hereafter 13b3mix) reproduces fairly well both L_{30} and the radioactive tail, but it is substantially brighter in the late stages of the plateau phase. Note also that, in both cases, there is a discrepancy between the observed and theoretical light curve in the first ~ 20 days. More specifically, the luminosity of the theoretical light curve decreases much faster than the observed one. This is a well-known problem that has been addressed in a number of quite recent papers (Moriya et al. 2017, 2018; Morozova et al. 2017, 2018, 2020; Paxton et al. 2018). In all of these studies, it has been shown that the presence of dense circumstellar material around the star should produce a better agreement between the theoretical and observed light curve in the first ~ 10 – 20 days. Since we do not address this problem in the present work, we will focus only on the light curve at times later than ~ 20 days and leave this subject for a future paper.

Figure 41 shows that the faster decline of the observed light curve in the transition phase from the plateau to the radioactive tail can be better reproduced by assuming a more efficient mixing of the chemical composition. The light curve of the model where we increase the number of iterations in the boxcar parameters (orange line in Figure 41) is closer to the observations but still rather brighter. Figure 42 shows the effect of changing the number of boxcar iterations on the interior composition of model 13b3. It is evident how the transition from the H- to the He-rich zone becomes progressively smoother as the number of boxcar iterations increases. Note that in the model with Iter = 10, the hydrogen is mixed down to the base of the ejecta. More efficient mixing also implies a longer plateau phase, and therefore the radioactive tail begins at later times, in this case, compared to the observations. The opposite effect is

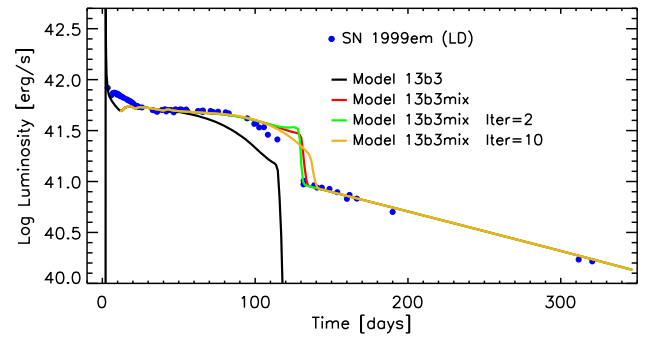


Figure 41. Dependence of the light-curve behavior on the mixing efficiency: model 13b3 (black line) is the reference model, model 13b3mix (red line) is the same as the reference model but in which $\sim 0.022 M_{\odot}$ of ^{56}Ni is deposited and homogeneously mixed up to a mass coordinate marking half of the H-rich envelope, and models 13b3mix Iter = 2 (green line) and 13b3mix Iter = 10 (orange line) are the same as 13b3mix but in which the number of iterations of the boxcar is two and 10, respectively. The blue dots refer to the observed bolometric light curve reported in the LD case (see text).

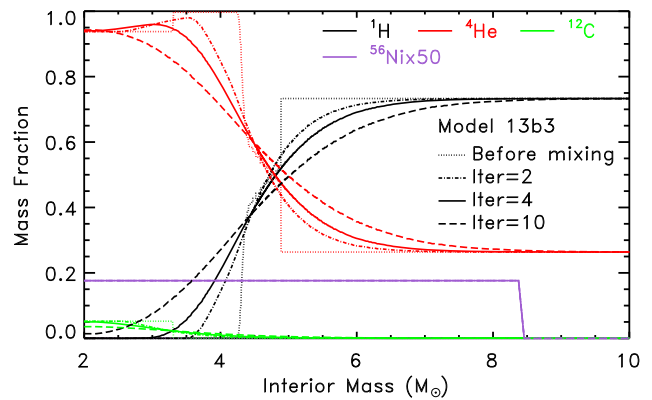


Figure 42. Interior profiles of selected isotopes (see legend) of model 13b3 obtained with different choices of the number of boxcar iterations: no mixing (dotted lines), Iter = 2 (dotted-dashed lines), Iter = 4 (solid lines); the reference value of all models reported in Table 3), and Iter = 10 (dashed lines). In all models, ^{56}Ni is homogeneously mixed from the inner edge of the ejecta up to half (in mass) of the H-rich envelope.

obtained by increasing the zone where ^{56}Ni is homogeneously mixed. The larger the zone, the earlier the end of the plateau phase and the smoother the transition from the plateau to the radioactive tail (Figure 43). Note that a spread of ^{56}Ni over a wider zone would determine a slight increase of L_{30} .

By combining more efficient mixing (Iter = 10) with a more extended zone where ^{56}Ni is homogeneously mixed (up to the surface), we obtain a good fit to the observations (model 13b3best; Figure 44). Although in this case, L_{30} increases slightly, this is still compatible with the observed one. A similar or even better fit to the observations can certainly be obtained with different choices of mixing parameters or by better tuning the explosion energy, but, given all of the uncertainties affecting both the observations and the models, we think that the fit shown in Figure 44 can be considered satisfactory.

The good fit to the light curve, however, does not imply a good fit to the observed photospheric velocity. Figure 45 shows that the photospheric velocity of the model that reproduces the observed light curve of SN 1999em (13b3best) is substantially lower than the observed one, especially at early times, which confirms the difference of the structure of the more external

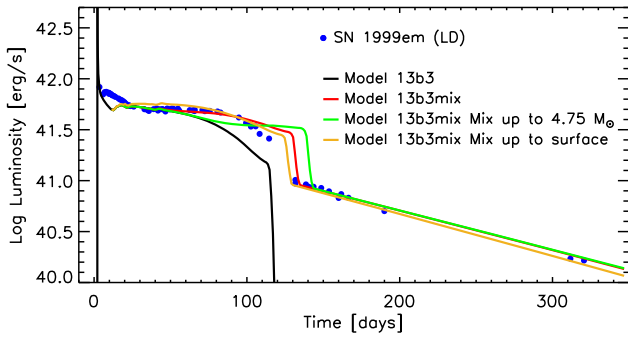


Figure 43. Dependence of the light-curve behavior on the outer edge of the zone where ^{56}Ni is homogeneously mixed; the black and red lines refer to models 13b3 and 13b3mix (see text), and the green and orange lines refer to the models where ^{56}Ni is homogeneously mixed up to a mass coordinate of $4.75 M_{\odot}$ and the surface, respectively. The blue dots refer to the observed bolometric light curve reported in the LD case (see text).

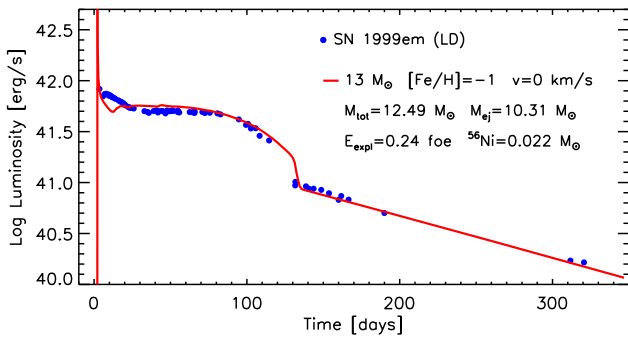


Figure 44. Light curve of a nonrotating model with initial mass $13 M_{\odot}$ and initial metallicity $[\text{Fe}/\text{H}] = -1$ (red line). The total mass of this star at the presupernova stage is $M_{\text{tot}} = 12.49 M_{\odot}$; after the explosion, the ejected mass is $M_{\text{ej}} = 10.31 M_{\odot}$ with a total explosion (mainly kinetic) energy of $E_{\text{expl}} = 0.24$ foe. The ^{56}Ni ejected is $0.022 M_{\odot}$. The blue dots refer to the observed bolometric light curve reported in the LD case (see text).

layers between the presupernova model and the real progenitor star. A better agreement is obtained for higher explosion energies. Figure 45 shows that the model with a final explosion energy of 1 foe reproduces the observations fairly well; however, its bolometric luminosity is substantially higher than the observed one. This problem has already been found and discussed by other studies, e.g., Utrobin et al. (2017; see their Figure 6(b)) and Morozova et al. (2020; see their Figure 3, right panel), and we find similar results. However, Paxton et al. (2018) showed that the evaluation of the velocity where the Sobolev optical depth of the Fe II is equal to 1 provides a much better match to the observations than the photospheric velocity. We do not address this problem in the present work, but since it is clearly important to find a simultaneous fit to both the light curve and the expansion velocity, we will address this issue in a forthcoming paper.

Let us now analyze the comparison between the LD case and model 13a1. As for model 13b3, in this case, the remnant mass is large enough ($M_{\text{rem}} = 3.00 M_{\odot}$) that a negligible amount of ^{56}Ni is ejected. Therefore, also in this case, we deposit in the model $0.022 M_{\odot}$ of ^{56}Ni . The light curve obtained in this case (13a1mix; green line in Figure 46) shows a plateau phase that lasts longer and a luminosity in the transition phase between the plateau and the radioactive tail that is higher than the observed ones. As has already been mentioned above, a

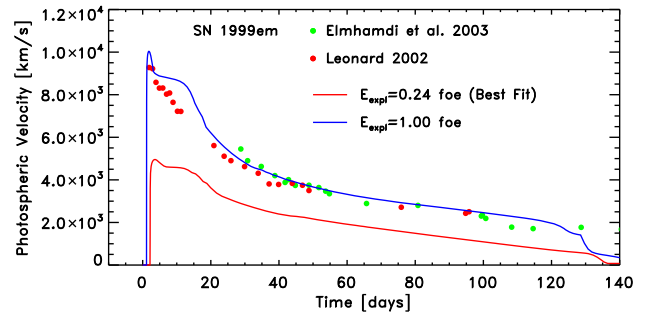


Figure 45. Radial velocities at maximum absorption of Fe II lines measured by Leonard (2002; red dots) and at maximum absorption of Sc II lines provided by Elmhamdi et al. (2003; green dots). The red line refers to the model 13b3best, while the blue line refers to the model with a final explosion energy of 1 foe.

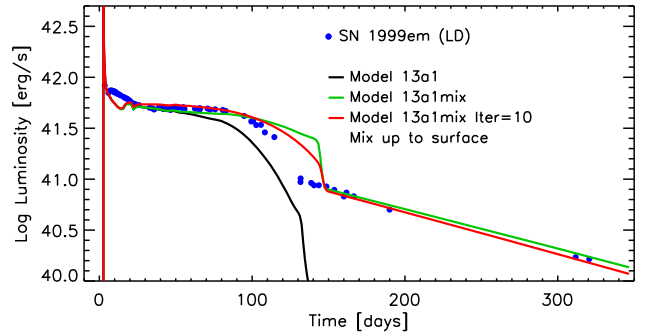


Figure 46. Light curves of a nonrotating model with initial mass of $13 M_{\odot}$, initial metallicity $[\text{Fe}/\text{H}] = 0$, and explosion energy of 0.2 foe. Black line: reference model (13a1; first line in Table 3). Green line: model 13a1mix, i.e., same as 13a1, where $0.022 M_{\odot}$ of ^{56}Ni is deposited and homogeneously mixed up to half of the H-rich envelope. Red line: model 13a1mix Iter = 10, i.e., same as 13a1mix with more efficient mixing (Iter = 10 in the boxcar parameters) and where ^{56}Ni is homogeneously mixed up to the surface. The blue dots refer to the observed bolometric light curve reported in the LD case (see text).

combination of more efficient mixing of the composition and a more extended zone where ^{56}Ni is homogeneously mixed produces a shorter plateau and smoother transition to the radioactive tail; therefore it should produce, in this case, a better agreement with the observations. The red line in Figure 46 is obtained assuming the same parameters adopted for model 13b3best, i.e., homogeneous mixing of ^{56}Ni up to the surface coupled with very efficient mixing of the chemical composition (Iter = 10). In spite of this more extended and vigorous mixing, Figure 46 shows that, in this case (red line), the plateau phase is still longer and brighter in the late stages compared to the observed one. Since this is the maximum efficiency of mixing that we can assume, we must conclude that model 13a1 cannot reproduce the light curve of SN 1999em (LD).

Summarizing the results discussed so far, we conclude that a nonrotating star with initial mass $13 M_{\odot}$ and metallicity $[\text{Fe}/\text{H}] = -1$ is compatible with the progenitor of SN 1999em when we adopt the lower distance (7.83 Mpc) to the host galaxy NGC 1637. However, a lower progenitor mass and/or explosion energy cannot be excluded.

In the higher-distance case (11.7 Mpc; HD), the observed $\log L_{30}$ is $\simeq 42.06$. Looking at Table 3 and Figure 36, for all of the progenitor models of series “a” and “b” with an initial mass lower than $25 M_{\odot}$, there exist explosions providing values of $\log L_{30}$ that bracket the observed value. Therefore, at variance

Table 4
Calculations with Different Choices of Mixing Parameters

Simulation ID	Iter	M_{out}
1	2	H/He interface
2	2	Half of the H-rich envelope
3	2	Surface
4	4	H/He interface
5	4	Half of the H-rich envelope
6	4	Surface
7	10	H/He interface
8	10	Half of the H-rich envelope
9	10	Surface

with the LD case, now the mass of the progenitor star spans larger values due to the higher intrinsic luminosity of the supernova. The selected models are the following: 13a2 and 13a3 (with $E_{\text{expl}} = 2.50 \times 10^{50}$ and 5.34×10^{50} erg, respectively), 15a3 and 15a4 (with $E_{\text{expl}} = 2.74 \times 10^{50}$ and 5.88×10^{50} erg, respectively), 13b4 (with $E_{\text{expl}} = 5.29 \times 10^{50}$ erg), 15b2 and 15b3 (with $E_{\text{expl}} = 2.44 \times 10^{50}$ and 5.91×10^{50} erg, respectively), and 20b3 and 20b4 (with $E_{\text{expl}} = 2.90 \times 10^{50}$ and 5.93×10^{50} erg, respectively). Due to the coarse grid in the explosion energies, we computed additional explosions by varying the explosion energy in order to obtain a $\log L_{30}$ that is closer to the observed one. Substantial fallback occurs in all of the previous models; therefore, in all of them, $0.05 M_{\odot}$ of ^{56}Ni is deposited and homogeneously mixed in order to reproduce the observed radioactive tail. As we have discussed above, once both the $\log L_{30}$ and the radioactive tail are reproduced, the shape of the light curve in the transition phase from the plateau to the radioactive tail depends mainly on the efficiency of the mixing of the chemical composition and the region where ^{56}Ni is homogeneously deposited. In order to be more systematic, once all of the other parameters are fixed (mass, metallicity, explosion energy, and total amount of ^{56}Ni deposited), we computed various explosions by changing the two parameters that control the efficiency of the chemical mixing and the extension of the zone where ^{56}Ni is homogeneously mixed. In particular, we named these explosions with the following rule: xxxZe.ee_n, where xxx refers to the mass (e.g., 013, 015, etc.); Z is the series in metallicity (e.g., a, b, c, d); ee means the explosion energy in foe (e.g., 0.50 means 0.50 foe); and n refers to the various simulations with different choices of mixing parameters (see Table 4), i.e., the number of iterations of the boxcar (Iter) and the outer mass coordinate of the zone where the ^{56}Ni is homogeneously mixed (M_{out}). The effect of changing the number of boxcar iterations (Iter = 2, 4, and 10) on the chemical composition for all models mentioned above is similar to the one already shown in Figure 42.

Figures 47–51 show the results for all of the models that simultaneously fit the observed $\log L_{30}$ and the radioactive tail with different choices of mixing parameters (as reported in Table 4).

Looking at these figures, we first conclude that all of the explosions where the ^{56}Ni is mixed up to the H/He interface (black lines) must be excluded. In these cases, in fact, during the plateau phase, all of the light curves show an initial decrease (until day 70–80) followed by a phase where the luminosity is constant or slightly increasing due to the energy

provided by the ^{56}Ni that eventually ends when the radioactive tail sets in. The observed light curve does not show such behavior, but, on the contrary, it is almost flat until day ~ 80 and then shows a smooth transition toward the radioactive tail.

Inspection of Figure 51 reveals that model 20b must be definitely excluded as a possible progenitor for 1999em. In fact, in all cases studied, the light curves are brighter in the transition phase, and the plateau is longer than the observed ones.

Model 13b must also be excluded, since in all cases, the luminosity of the plateau between days 70 and 90 is lower than the observed one.

In all other cases, i.e., 13a, 15a, and 15b, there exists at least one case, or even more than one, that is compatible with the observations within all of the theoretical and observation uncertainties. In general, the models that better reproduce the shape of the observed light curve in the transition phase are those with moderate mixing of the chemical composition (middle panels in Figures 47, 48, and 50) and the region where the ^{56}Ni is homogeneously mixed extending up to half of the H-rich envelope. In spite of this general rule, there are cases where less extended mixing of the chemical composition or a more extended zone where ^{56}Ni is mixed cannot be excluded.

Information on the photospheric velocity could provide an additional constraint on the progenitor star. Therefore, we show in Figures 52–54 the comparison between the predicted and observed photospheric velocities for models 13a, 15a, and 15b, corresponding to those reported in Figures 47, 48 and 50. In the abovementioned figures, each line refers to a model computed with a given explosion energy, regardless of the mixing parameters. The reason is that the photospheric velocity does not depend on the mixing parameters but only on the explosion energy. In this case, a discrepancy between observed and predicted photospheric velocity similar to the LD case is found. However, the higher distance to SN 1999em implies a higher $\log L_{30}$ and therefore an explosion energy for the same progenitor mass. As a consequence, in this case, the discrepancy mentioned above reduces compared to the LD case (Figure 45).

Since there is no strict rule on the basis of which we can definitely say which is the model that best fits the observed light curve, we leave this exercise to the reader and draw a more general conclusion. In particular, we conclude that, in the HD case, the models $13 M_{\odot}$ (with $[\text{Fe}/\text{H}] = 0$ and $E_{\text{expl}} \sim 5 \times 10^{50}$ erg), $15 M_{\odot}$ (with $[\text{Fe}/\text{H}] = 0$ and $E_{\text{expl}} \sim 3 \times 10^{50}$ erg), and $15 M_{\odot}$ (with $[\text{Fe}/\text{H}] = -1$ and $E_{\text{expl}} \sim 4 \times 10^{50}$ erg) are, in principle, all compatible with the progenitor star of SN 1999em.

6. Conclusions

In this paper, we presented and described in detail the latest version of the HYPERION code. HYPERION is designed to calculate the explosive nucleosynthesis, remnant mass, and bolometric light curve associated with the explosion of a massive star. The core of HYPERION is based on a previous hydro code, which has been extensively used for explosive nucleosynthesis calculations (Limongi & Chieffi 2006, 2012; Chieffi & Limongi 2013, 2017; Limongi & Chieffi 2018). It is based on a PPM scheme with a Riemann solver (Colella & Woodward 1984) coupled with a fully automated nuclear network including 339 nuclear species and more than 3000 nuclear reactions (Limongi & Chieffi 2018). With respect to the

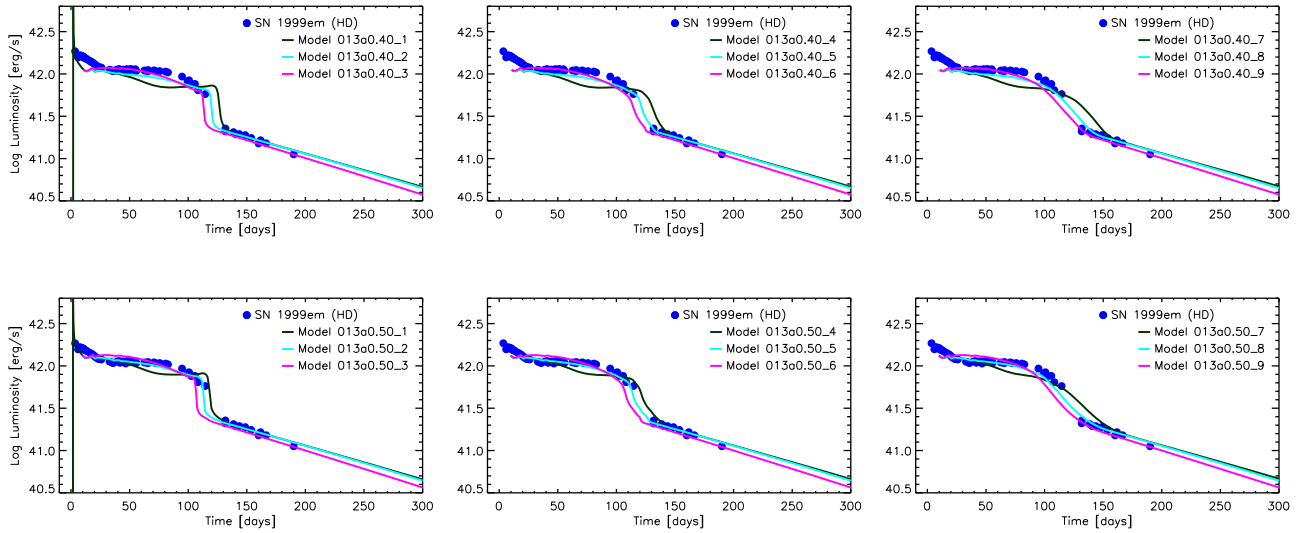


Figure 47. Light curves for model 13a obtained for different values of the explosion energies (0.40 and 0.50 foe in the upper and lower rows, respectively) and mixing parameters (see Table 4). In all cases, $0.05 M_{\odot}$ of ^{56}Ni is deposited and homogeneously mixed.

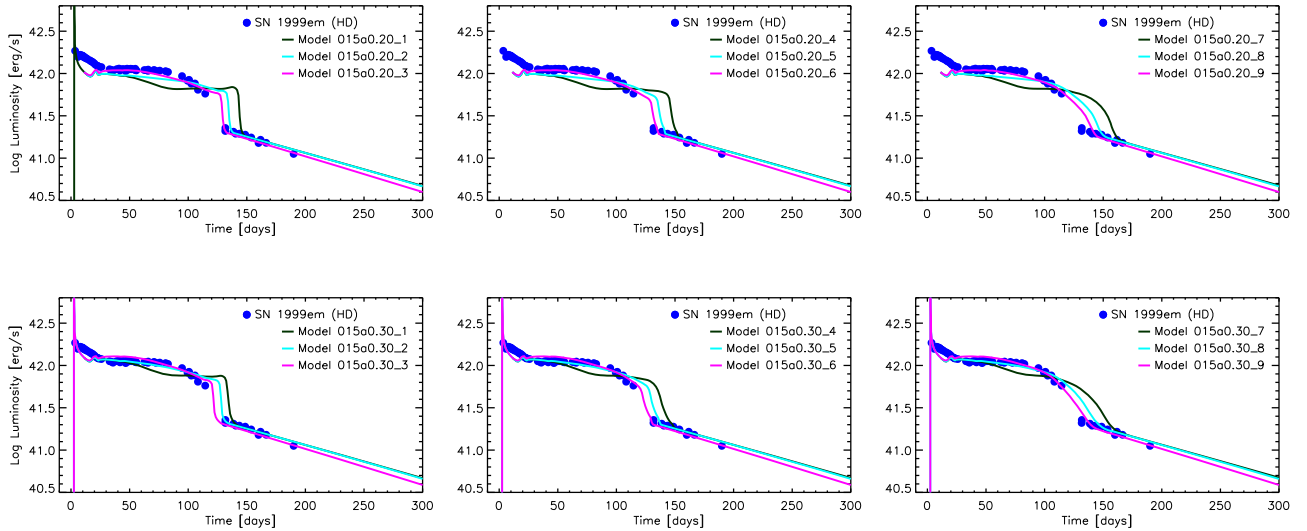


Figure 48. Same as Figure 47 but for model 15a.

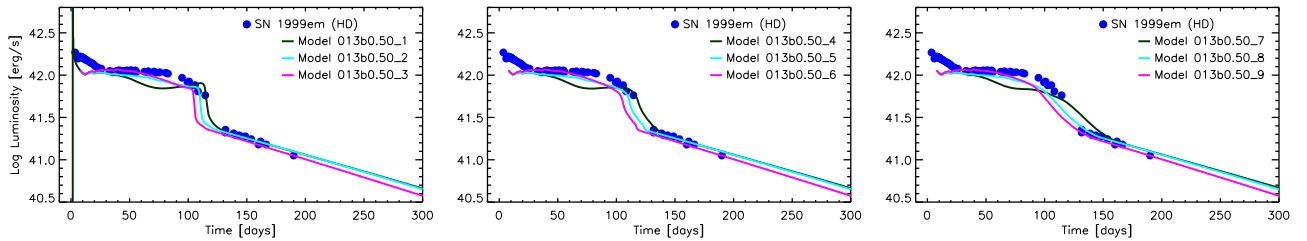


Figure 49. Same as Figure 47 but for model 13b.

previous version, HYPERION includes the radiation transport in the flux-limited diffusion approximation and therefore allows the calculation of the bolometric light curve.

By means of this code, we computed a set of explosions and associated explosive nucleosynthesis and bolometric light curves for a subset of nonrotating presupernova models that retain their H-rich envelope, taken from the database published

in Limongi & Chieffi (2018). All of the explosions are induced by instantaneously depositing some amount of thermal energy within the Fe core. The energy deposited is chosen in order to have a given final explosion energy. All of the simulations are followed until 10^7 s. In this way, the physical and chemical properties of the progenitor star, e.g., the envelope mass; total radius; interior profiles of the temperature, density, and

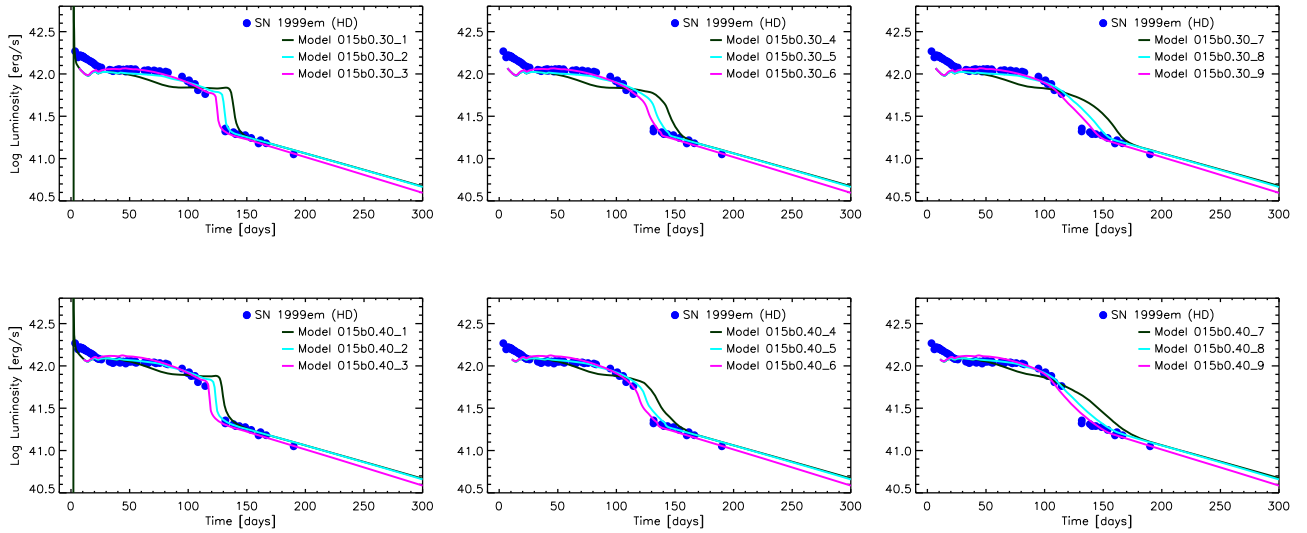


Figure 50. Same as Figure 47 but for model 15b.

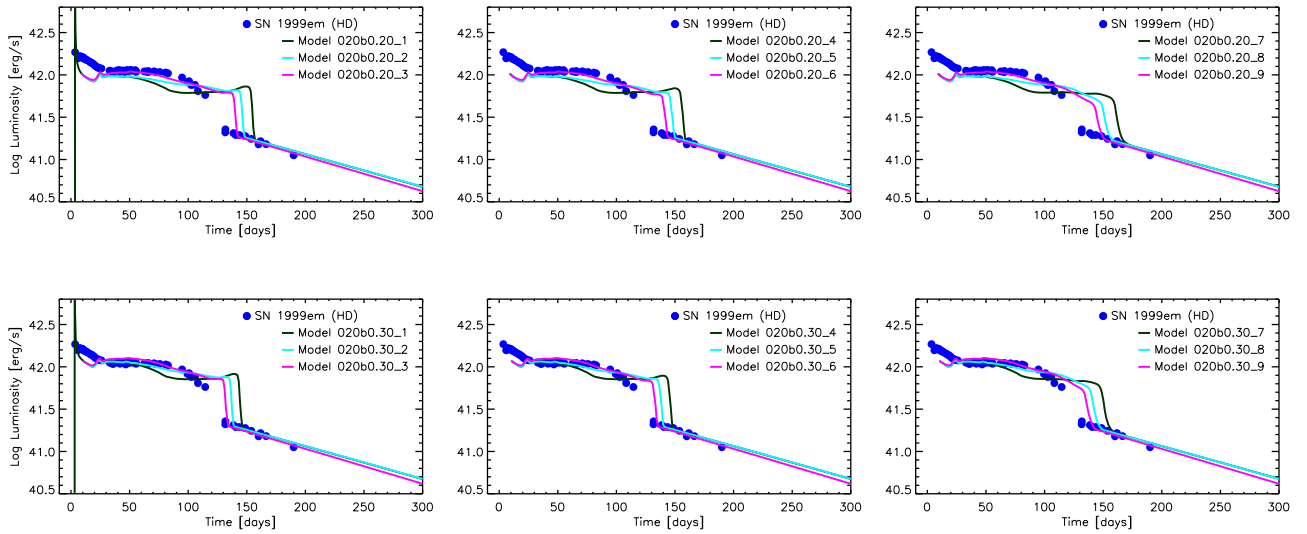


Figure 51. Same as Figure 47 but for model 20b.

chemical composition; and so on are not treated as free parameters but, on the contrary, are the result of the evolution of the star as a function of initial mass and metallicity (in general, they also depend on the initial rotation velocity).

As a first check of HYPERION, we have deeply analyzed and described in detail the results obtained for a typical case, i.e., a solar metallicity nonrotating $15 M_{\odot}$ model with a final explosion energy of 1 foe. All of the phases characterizing the light curve have been discussed in detail, and special attention has been devoted to the luminosity “bump” that characterizes the light curve in the transition phase between the plateau and the radioactive tail. Since this feature has never been observed in SN IIP light curves, we studied in detail such a phenomenon and concluded that this characteristic is mainly due to the drop in the opacity within the He core when He recombines. In order to minimize such a sharp variation of the opacity, we made additional tests to verify the sensitivity of the bump to the mixing of both the density and the chemical composition. In fact, it is quite probable that in more realistic

3D calculations, both of these quantities could be significantly smoothed with respect to the 1D simulations. The result of these tests was that with a proper combination of the smoothing of the density gradient and the mixing of both the chemical composition and the ^{56}Ni , the bump in the light curve disappears. It must be noted, however, that we are dealing with a feature that corresponds to a very small variation of the luminosity (of the order of $\sim 5\%$).

The full set of calculations allowed us to study the main outcomes of the explosions as a function of the progenitor mass, initial metallicity, and explosion energy. In particular, we focused on the remnant mass, ejected amount of ^{56}Ni , luminosity after 30 days, and duration of the plateau of the light curve. In general, as the explosion energy decreases, the remnant mass increases, and, as a consequence, the amount of ^{56}Ni decreases as well. This is a consequence of the fact that the larger the initial mass, the larger the binding energy of the core, and also that the ^{56}Ni is produced in the innermost zones of the exploding mantle. For this reason, for each progenitor

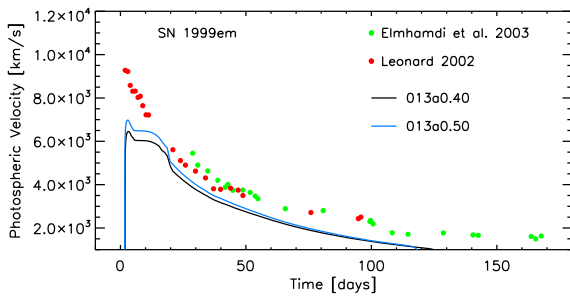


Figure 52. Radial velocities at maximum absorption of Fe II lines measured by Leonard (2002; red dots) and at maximum absorption of Sc II lines provided by Elmhamdi et al. (2003; green dots). The black and blue lines refer to models 013a0.40 and 013a0.50 (see the text), respectively.

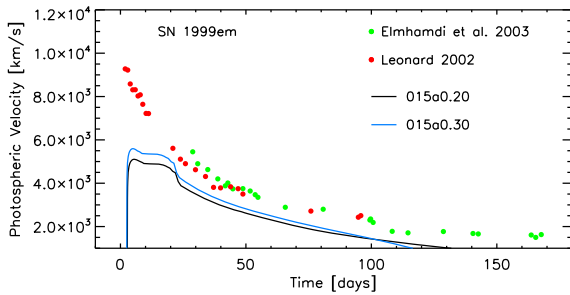


Figure 53. Same as Figure 52 but for models 015a0.20 and 015a0.30.

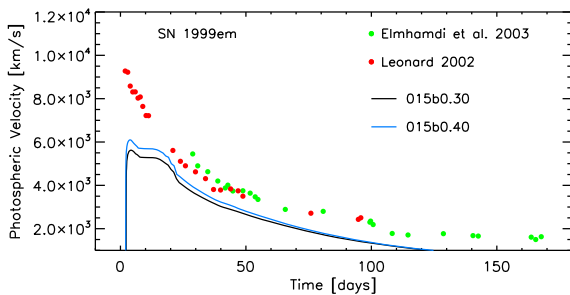


Figure 54. Same as Figure 52 but for models 015b0.30 and 015b0.40.

mass and initial metallicity, we found a critical value of the explosion energy below which the light curve does not show the radioactive tail. The other important result was that larger remnant masses are obtained for lower metallicities, the reason being that as the metallicity decreases, the dramatic reduction of the mass loss implies larger CO cores and therefore larger binding energies for the same progenitor mass.

The luminosity of the plateau, evaluated 30 days after the shock breakout, $\log L_{30}$, varies between ~ 41.6 and ~ 42.7 in the range of parameters. We found that, for any initial metallicity, $\log L_{30}$ increases significantly with the explosion energy. On the other hand, for any fixed explosion energy, $\log L_{30}$ decreases with decreasing the initial metallicity. Note that the luminosity evaluated at early times is almost independent of the amount and degree of mixing of ^{56}Ni .

The length of the plateau depends on both the explosion energy and the ^{56}Ni ejected; therefore, it shows nonmonotonic behavior in the whole range of explosion energies, progenitor masses, and initial metallicities. In general, the length of the

plateau decreases with increasing the explosion energy as long as the ^{56}Ni ejected is lower than $\sim 10^{-3} M_{\odot}$. For higher values of this last quantity, the plateau duration starts increasing as the explosion energy progressively increases until a maximum value is reached, after which it starts decreasing again.

As a first application of this code, we presented a fit to the observed bolometric light curve of SN 1999em. We chose SN 1999em because it is one of the most widely studied SNe IIP, and it is often considered as a template for this kind of supernova. Since the distance to the supernova host galaxy, i.e., NGC 1637, is still under debate, we studied the two extreme cases where the distance is assumed, 7.83 (LD) and 11.8 (HD) Mpc, respectively. We presented our fitting strategy, which can be summarized through the following steps. (1) We select the progenitors with both metallicity and $\log L_{30}$ closer to the observed values; iterations on the explosion energy could be necessary to refine the fit to the observed $\log L_{30}$. (2) We change the amount of ^{56}Ni ejected in order to fit the radioactive tail; the basic assumption in this step is that in more realistic 3D simulations, ^{56}Ni -rich bubbles are pushed outward in mass before the occurrence of the fallback. (3) We study the efficiency and extension of the mixing of both the chemical composition and the ^{56}Ni in order to reproduce the transition phase between the plateau and the radioactive tail; also in this case, the assumption at the basis of this step is that we expect a substantial degree of mixing during multidimensional simulations. The result of the fitting procedure was that in the LD case, we exclude all progenitors with masses larger than $13 M_{\odot}$ and metallicities $[\text{Fe}/\text{H}] \geq 0$ and ≤ -2 . Note that metallicities $[\text{Fe}/\text{H}] \leq -2$ are excluded a priori because the metallicity of NGC 1637 has been estimated of the order of $[\text{Fe}/\text{H}] \sim -0.33$. Therefore, we conclude that a nonrotating star with mass $M = 13 M_{\odot}$ and metallicity $[\text{Fe}/\text{H}] = -1$ is compatible with the progenitor of SN 1999em (in the LD case). Progenitors with metallicities in the range $0 > [\text{Fe}/\text{H}] > -1$ or an initial mass lower than $13 M_{\odot}$ cannot be studied because of the coarse grid of presupernova models in both the metallicities and the initial masses. The analysis of the radial velocities shows the existence of a discrepancy between the fit to the light curve and the fit to the photospheric velocity. In particular, the energy required to fit the light curve, in particular the value of $\log L_{30}$, is substantially lower (by about a factor of 2) than the one required to fit the photospheric velocity. This problem has already been found by other authors, e.g., Utrobin et al. (2017), when the adopted presupernova model is the result of the stellar evolution calculations. Paxton et al. (2018), however, showed that the evaluation of the velocity where the Sobolev optical depth of Fe II is equal to 1 provides a much better agreement with the observations. In the HD case, the supernova is intrinsically more luminous; therefore, the progenitor mass can be as high as $15 M_{\odot}$. In particular, we find that models with metallicity $[\text{Fe}/\text{H}] = 0$ in the mass range $13\text{--}15 M_{\odot}$ and $[\text{Fe}/\text{H}] = -1$ with a mass of $15 M_{\odot}$ are all compatible with the progenitor of SN 1999em. Also in this case, we find a discrepancy between the fit to the light curve and the fit to the photospheric velocity. However, due to the higher intrinsic luminosity, such a discrepancy is slightly reduced in this case compared to the LD case. In both cases (LD and HD), the predicted progenitor mass is compatible with other estimates available in the literature based on the preexplosion images of the supernova site (Smartt et al. 2002) or an analysis similar to the one described in this paper (Utrobin et al. 2017).

The results shown in this paper are encouraging, and a similar analysis of a more extended set of bolometric light curves will soon be presented in a companion paper.

We thank Stefano Benetti, Lina Tomasella, and Nando Patat for providing the observed bolometric light-curve data of SN 1999em and for useful and clarifying discussions. This work has been partially supported by the Italian grants “GRAWITA” (PI: E. Brocato), “Premiale 2015 MITiC” (PI: Bianca Garilli), and “Premiale 2015 FIGARO” (PI: Gianluca Gemme) and the “ChETEC” COST Action (CA16117), supported by COST (European Cooperation in Science and Technology).

ORCID iDs

Marco Limongi  <https://orcid.org/0000-0003-0636-7834>

Alessandro Chieffi  <https://orcid.org/0000-0002-3589-3203>

References

- Anderson, J. P., González-Gaitán, S., Hamuy, M., et al. 2014, *ApJ*, 786, 67
- Arnett, W. D. 1988, *ApJ*, 331, 377
- Asplund, M., Grevesse, N., Sauval, A. J., & Scott, P. 2009, *ARA&A*, 47, 481
- Aufderheide, M. B., Baron, E., & Thielemann, F.-K. 1991, *ApJ*, 370, 630
- Baklanov, P. V., Blinnikov, S. I., & Pavlyuk, N. N. 2005, *ASL*, 31, 429
- Baron, E., Nugent, P. E., Branch, D., et al. 2004, *ApJL*, 616, L91
- Bersten, M. C., Benvenuto, O., & Hamuy, M. 2011, *ApJ*, 729, 61
- Blinnikov, S., Lundqvist, P., Bartunov, O., et al. 2000, *ApJ*, 532, 1132
- Brodie, J. P., & Huchra, J. P. 1991, *ApJ*, 379, 157
- Cayrel, R., Depagne, E., Spite, M., et al. 2004, *A&A*, 416, 1117
- Chieffi, A., Domínguez, I., Höflich, P., et al. 2003, *MNRAS*, 345, 111
- Chieffi, A., & Limongi, M. 2004, *ApJ*, 608, 405
- Chieffi, A., & Limongi, M. 2013, *ApJ*, 764, 21
- Chieffi, A., & Limongi, M. 2017, *ApJ*, 836, 79
- Chieffi, A., Limongi, M., & Straniero, O. 1998, *ApJ*, 502, 737
- Colella, P., & Woodward, P. R. 1984, *JCoPh*, 54, 174
- Davies, B., & Beasar, E. R. 2018, *MNRAS*, 474, 2116
- Dessart, L., & Hillier, D. J. 2006, *A&A*, 447, 691
- Dessart, L., & Hillier, D. J. 2019, *A&A*, 625, A9
- Eastman, R. G., Schmidt, B. P., & Kirshner, R. 1996, *ApJ*, 466, 911
- Elmhamdi, A., Danziger, I. J., Chugai, N., et al. 2003, *MNRAS*, 338, 939
- Falk, S. W., & Arnett, W. D. 1977, *ApJS*, 33, 515
- Ferguson, J. W., Alexander, D. R., Allard, F., et al. 2005, *ApJ*, 623, 585
- Grassberg, E. K., Imshennik, V. S., & Nadyozhin, D. K. 1971, *Ap&SS*, 10, 28
- Hamuy, M., Pinto, P. A., Maza, J., et al. 2001, *ApJ*, 558, 615
- Heger, A., & Woosley, S. E. 2010, *ApJ*, 724, 341
- Huebner, W. F., Merts, A. L., Magee, N. H., & Argo, M. F. 1977, Los Alamos Scientific Laboratory Report (LA-6760-M)
- Iglesias, C. A., & Rogers, F. J. 1996, *ApJ*, 464, 943
- Itoh, N., Mitake, S., Iyetomi, H., et al. 1983, *ApJ*, 273, 774
- Jones, M. I., Hamuy, M., Lira, P., et al. 2009, *ApJ*, 696, 1176
- Kasen, D., & Woosley, S. E. 2009, *ApJ*, 703, 2205
- Kirshner, R. P., & Kwan, J. 1974, *ApJ*, 193, 27
- Kwan, J., & Thuan, T. X. 1974, *ApJ*, 194, 293
- Leonard, D. C. 2002, *PASP*, 114, 1291
- Leonard, D. C., Filippenko, A. V., Ardila, D. R., et al. 2001, *ApJ*, 553, 861
- Leonard, D. C., Kanbur, S. M., Ngeow, C. C., et al. 2003, *ApJ*, 594, 247
- Levermore, C. D., & Pomraning, G. C. 1981, *ApJ*, 248, 321
- Li, W. D. 1999, *IAUC*, 7294, 1
- Limongi, M., & Chieffi, A. 2003, *ApJ*, 592, 404
- Limongi, M., & Chieffi, A. 2006, *ApJ*, 647, 483
- Limongi, M., & Chieffi, A. 2012, *ApJS*, 199, 38
- Limongi, M., & Chieffi, A. 2018, *ApJS*, 237, 13
- Limongi, M., Straniero, O., & Chieffi, A. 2000, *ApJS*, 129, 625
- Maguire, K., Di Carlo, E., Smartt, S. J., et al. 2010, *MNRAS*, 404, 981
- Maguire, K., Kotak, R., Smartt, S. J., et al. 2010, *MNRAS*, 403, L11
- Martinez, L., & Bersten, M. C. 2019, *A&A*, 629, A124
- Moriya, T. J., Förster, F., Yoon, S.-C., et al. 2018, *MNRAS*, 476, 2840
- Moriya, T. J., Yoon, S.-C., Gräfener, G., et al. 2017, *MNRAS*, 469, L108
- Morozova, V., Piro, A. L., Fuller, J., et al. 2020, *ApJL*, 891, L32
- Morozova, V., Piro, A. L., Renzo, M., et al. 2015, *ApJ*, 814, 63
- Morozova, V., Piro, A. L., & Valenti, S. 2017, *ApJ*, 838, 28
- Morozova, V., Piro, A. L., & Valenti, S. 2018, *ApJ*, 858, 15
- Nadyozhin, D. K. 1994, *ApJS*, 92, 527
- Nugent, P., Sullivan, M., Ellis, R., et al. 2006, *ApJ*, 645, 841
- Paczynski, B. 1983, *ApJ*, 267, 315
- Paxton, B., Schwab, J., Bauer, E. B., et al. 2018, *ApJS*, 234, 34
- Pooly, D., Lewin, W. H. G., Fox, D. W., et al. 2001, American Astronomical Society Meeting Abstracts, 198, 8005
- Poznanski, D., Nugent, P. E., & Filippenko, A. V. 2010, *ApJ*, 721, 956
- Pumo, M. L., & Zampieri, L. 2011, *ApJ*, 741, 41
- Smartt, S. J., Gilmore, G. F., Tout, C. A., et al. 2002, *ApJ*, 565, 1089
- Sohn, Y.-J., & Davidge, T. J. 1998, *AJ*, 115, 130
- Spite, M., Cayrel, R., Plez, B., et al. 2005, *A&A*, 430, 655
- Sukhbold, T., Ertl, T., Woosley, S. E., et al. 2016, *ApJ*, 821, 38
- Swartz, D. A., Sutherland, P. G., & Harkness, R. P. 1995, *ApJ*, 446, 766
- Thielemann, F.-K., Nomoto, K., & Hashimoto, M.-A. 1996, *ApJ*, 460, 408
- Tomasella, L., Cappellaro, E., Fraser, M., et al. 2013, *MNRAS*, 434, 1636
- Tomasella, L., Cappellaro, E., Pumo, M. L., et al. 2018, *MNRAS*, 475, 1937
- Umeda, H., & Nomoto, K. 2002, *ApJ*, 565, 385
- Umeda, H., & Yoshida, T. 2017, in Handbook of Supernovae, ed. A. Alsabti & P. Murdin (Cham: Springer), 1753
- Utrobin, V. P. 2007, *A&A*, 461, 233
- Utrobin, V. P., & Chugai, N. N. 2008, *A&A*, 491, 507
- Utrobin, V. P., & Chugai, N. N. 2009, *A&A*, 506, 829
- Utrobin, V. P., Wongwathanarat, A., Janka, H.-T., & Müller, E. 2017, *ApJ*, 846, 37
- Woosley, S. E. 1988, *ApJ*, 330, 218
- Woosley, S. E., & Weaver, T. A. 1995, *ApJS*, 101, 181
- Zaghloul, M. R., Bourham, M. A., & Doster, J. M. 2000, *JPhD*, 33, 977